



Identification of geochemical anomalies associated with Cu mineralization by applying spectrum-area multi-fractal and wavelet neural network methods in Shahr-e-Babak mining area, Kerman, Iran

B. Shokouh Saljoughi and A. Hezarkhani*

Department of Mining and Metallurgy Engineering, Amirkabir University of technology (Tehran Polytechnic), Tehran, Iran

Received 7 April 2018; received in revised form 20 July 2018; accepted 21 July 2018

Keywords

Geochemical Anomaly
Wavelet Neural Network
Spectrum-Area Multi-Fractal Model
Cu Mineralization
Shahr-e-Babak

Abstract

The Shahr-e-Babak district, as the studied area, is known for its large Cu resources. It is located in the southern side of the Central Iranian volcano-sedimentary complex in SE Iran. Shahr-e-Babak is currently facing a shortage of resources, and therefore, mineral exploration in the deeper and peripheral spaces has become a high priority in this area. This work aims to identify the geochemical anomalies associated with the Cu mineralization using the Spectrum-Area (S-A) multi-fractal and Wavelet Neural Network (WNN) methods. At first, the Factor Analysis (FA) is applied to integrate the multi-geochemical variables of a regional stream sediment dataset related to major mineralization elements in the studied area. Then the S-A model is applied to decompose the mixed geochemical patterns obtained from FA and compare with the results obtained from the WNN method. The S-A model, based on the distinct anisotropic scaling properties, reveals the local anomalies due to the consideration of the spatial characteristics of the geochemical variables. Most of the research works show that the capability (i.e. classification, pattern matching, optimization, and prediction) of an ANN considering its successful application is suitable for inheriting uncertainties and imperfections that are found in mining engineering problems. In this paper, an alternative method is presented for mineral prospecting based on the integration of wavelet theory and ANN or wavelet network. The results obtained for the WNN method are in a good agreement with the known deposits, indicating that the WNN method with Morlet transfer function consists of a highly complex ability to learn and track unknown/undefined complicated systems. The hybrid method of FA, S-A, and WNN employed in this work is useful to identify anomalies associated with the Cu mineralization for further exploration of mineral resources.

1. Introduction

One of the most important aspects in the field of mineral exploration and environmental studies is to define and separate anomaly from the background [1, 2]. The separation of geochemical anomalies from the background has a profound influence on the analysis of geological evolutions and mineralization processes [3, 4]. Since geochemical elements provide important and direct clues related to the presence of mineral deposits, the geochemical anomalies play a significant role in mineral exploration [5, 6].

Moreover, the delineated anomalies are efficiently used in more advanced exploration-focused modellings such as GIS-based prospectively mapping [3, 7, 8].

A geochemical anomaly is a region where the concentration of a specific element is greater than a certain threshold value [9, 10]. It occurs by various natural processes related to different geological events such as tectonics and mineralization [11, 12]. Geological phenomena are inherently complex, and many features show

✉ Corresponding author: ardehez@aut.ac.ir (A. Hezarkhani).

that several processes have taken place, overprinting each other, and crafting one another's present appearance. It is considered as a simple feedback system, in which at least a part of the process output turns into the input of the same or a different process within the geological sequence of events [13-17]. Geochemical distributions are no exception, and formation of the geochemical anomalies often indicates the retreat of the former chemically anomalous volumes of rocks, in which the efficiency of the processes themselves such as the supergene enrichment of the ore deposits is enhanced. This leads to very complex distribution patterns of the chemical elements within the crust or even on the earth's surface [18]. Therefore, areas with disparate anomalies (or baseline) and backgrounds demonstrate a mixed pattern due to the superposition of different geological processes or events. According to the mentioned issues such as importance of isolating the geochemical anomalies and the complexity of geochemical patterns, the main challenge for exploration geochemists is to apply transparent and robust geochemical exploration techniques for decomposing mixed geochemical patterns and mapping.

In order to separate the geochemical anomalies from the background, emerging computational geoscience methods have been developed in the recent years within extensive and systematic studies. The fundamental requirement of geochemical data processing is to determine the threshold to separate anomalies from the geochemical background and then delineate the mineralized areas or distinguish the anthropogenic and natural sources of the materials [19, 20]. In general, separation of geochemical anomalies from the background consists of the following aspects: frequency distribution, spatial correlation and variability, geometrical characteristics of the anomalies, and scale of independence properties [5, 6]. Based on the number of utilized thresholds in the studied area, the techniques are classified into two categories: (i) hard threshold techniques such as mean plus two or three times of a variable's standard deviation, and (ii) soft threshold techniques such as spectrum and area model (S-A model) [21]. On the other hand, according to the frequency and spatial distributions, the methods are broadly categorized into non-structural (frequency-based), statistical, structural (spatial frequency-based), and spatial [22-25]. Statistical methods such as histograms and Q-Q plots [26, 27], probability graphs [19, 22,

28], exploration data analysis (EDA) [29, 30], box-plots [19, 31, 32], mean \pm 2SD (Standard Deviation) [20, 33], median+2MAD (Median Absolute Deviation) [19, 33], fence method [31, 33], and multivariate analysis methods [3, 34-36] are primarily concerned with the frequency distribution of the element concentration values and relations between multiple variables. These methods are regarded as non-spatial statistical tools in which the spatial information and the spatial autocorrelation structure of the geochemical data are neglected. Statistical methods are sufficient in separating the background populations and anomalies within simple geological settings. However, their efficiency is limited in complex geological areas, where different geological processes coincide spatially and temporally to form complex geochemical distributions [37, 38]. Due to that, applying the traditional methods to determine threshold values leads to an inaccurate identification of geochemical anomalies. Therefore, the spatial models are developed for mapping geochemical anomalies. These methods such as moving average technique [39], conditional simulation [39], Fourier filtering [10], wavelet filtering techniques [40], spatial factor analysis, [41] and spatial U-statistics [37] consider both the spatial correlation and variability within neighboring samples in addition to the concentration value frequency distributions and correlation coefficients. The spatial methods are effective in solving problems but where there is an extensive overlap between the background and anomalous values or weak anomalous values are hidden within the strong variance of the background, the applicability of these methods are limited [8, 42]. Anomalous patterns caused by the mineralization processes are highly complex regarding their spatial and frequency properties. The proper quantification of these spatial and spectral properties is essential to identify weak or complex anomalies.

Since Mandelbrot has expressed the concept of fractals more than two decades ago [43], the fractal and multi-fractal models have been applied to physical and chemical quantities with geometrical support. Examples include box counting model [43, 44], Concentration–Area model (C–A) [23, 24, 37, 45], Spectrum–Area (S–A) model [46, 47], Multi-fractal Singular Value Decomposition (MSVD) [11, 12, 48], Concentration–Distance (C–D) model [9], Number–Size (N–S) model [1, 4, 49], singularity

mapping technique [3, 50], multi-fractal model [51-52], and many other applications.

As mentioned earlier, many geological phenomena such as mineralization and geochemical dispersion patterns are inherently complex and exhibit high variations and strong non-linearity over a wide range of spatial scales [53]. Furthermore, there is a non-linear and complex relationship between the geochemical variables and the mineral resources [38]. Understanding these relationships leads to more efficient mineral exploration. Lots of research works have shown that ANN, considering its successful application and ability to classification, pattern matching, prediction, and data mining, is capable of addressing the inherit uncertainties and imperfections found in exploratory geochemical problems [38, 54-55]. Moreover, ANN has a significant ability to find the complex spatial relationship between the different geochemical variables and also between the variable and occurrence/deposit location.

The Shahr-e-Babak district, located in SW Iran, is known for its large Cu resources, yet is currently facing a shortage of the mentioned deposit. The geochemical surface and geological/tectonic setting of Shahr-e-Babak is complex. In this work, a hybrid approach involving the factor analysis (FA) and a spectrum–area (S–A) fractal model aided by the wavelet neural network (WNN) was applied to separate the mixed geochemical anomalies associated with the Cu mineralization based on the stream sediment data in the Shahr-e-Babak district. The main goals of this work were to characterize the Cu-related element associations, identify the geochemical anomaly patterns, and examine the non-linear relationships between the geochemical variables and mineral resources by the proposed methodology that provides vectors to mineral resource exploration.

This paper is organized as what follows. In Section 2, the studied area is investigated according to the regional geology, structural geology, and geological setting. In Section 3, the geochemical dataset and statistical calculations are described. An overview of the methods, their principles, advantages, and limitations are described in Section 4. The results obtained are discussed in Section 5. Finally, in Section 6, conclusions are presented.

2. Description of studied area

The studied area is located in the southern side of the Central Iranian Volcanic Sedimentary Complex (Iran). The NE part of the area is

mountainous. It composes of Paqaleh range in the east, prominent volcano of Kuh-e-Mosahim in the central part, and Narkuh in the NW area. The Dasht plain of Shahr-e-babak (Dasht-e Yekkeh Baneh) with an altitude between 1800 and 2000 m is spread in the south and SW of this area. The drainage pattern is centrifugal in the mountains and mostly parallel in the Dasht plain. The most important watercourse of the area is Rud-e Kang, located at the west side. The prevailing part of the sheet territory is drained to SW [56]. Regarding a regional Cu potential analysis in the Shahr-e-Babak district, the studied area was chosen as a high mineral potential. This region contains many mineral occurrences, while the geological, geochemical, and geophysical survey data is available.

The geological map of the studied area is shown in Figure 1, which is based upon the geological mapping carried out by the Yugoslavian group in 1970s. The oldest units are Cretaceous sediments located at the northernmost part of the sheet (Cenomanian-Turonian flysch often with bioglyphs) and colored *mélange* formation in the southern side [56].

The flysch sediments of the Eocene age occurred in the core of the denuded open-anticline axis running NW-SE in the northern part of the studied area. The Eocene volcanic-sedimentary is the most significant geological unit in the area, which is composed of 80% of pyroclastics, 10% of lava flows, and a remaining 10% of sediments [56].

This huge volcano-sedimentary sequence (at least with a thickness of 15 Km) is divided into the Bahr Aseman, Razak, and Hezar complexes by Dimitrijevic (1973) [57]:

- The Lower Eocene Bahr Aseman complex begins with several meters of basal arenites, Pyroclastics, rhyolite, trachyandesite, andesite, and rhyolite flows.
- The Razak complex overlies the Middle Eocene sedimentary sequence. It is divided into 3 units. The lower and upper volcanic units are mainly basic, while the middle one is acidic.
- The Hezar complex represents the youngest phase of Eocene volcanic activity. It is composed of rapidly alternated andesite-basalt, andesite, and rhyolite lava flows.

This sequence in intrusions dated to Miocene (probably in the time span of uppermost Oligocene to Upper Miocene). Igneous rocks are categorized into two units [57]:

- Granodiorite rocks of Jebal Barez type (granite, granodiorite, quartz diorite, monzonite,

and syenite), which are represented by the Chenar massif and several smaller intrusions.

- Kuh-e-Panj type consists of sub-volcanic rocks of a porphyritic character and a strong diversity in composition (quartz diorite, diorite, dacite, etc.). The volcanic necks determined as “dacite and andesite” in the area also belong to this type.

The activity of the Kuh-e-Mosahim central volcano started regarding the pyroclastic explosion and continued with deposition of a predominantly pyroclastic material with only several andesite lava flows. Small diorite bodies and dykes are cropped out in strongly altered rocks in the caldera.

Numerous dykes with NW-SE strike occurred in the area. The N-S and E-W strikes were predominant in the northern and eastern parts of the studied area, respectively. According to some contacts, the dykes belonged to Eocene up to the youngest volcanic activity of the Pliocene. The composition of the dykes is very variable but the dacite and andesite dykes are prominent [56].

Regarding the structural geology, the position of Eocene and Cretaceous flysch in the north-center part of the studied area can be interpreted as the core of “open” anticline in regional scale. The Dehno fault separates the Eocene flysch and

volcanics in the southwestern flank. The parallel zone of weakness about 10 km southwestward confirmed by the airborne measurements (Vukasinovic S., Aeroradiometric map, in [57]) implicates anomalous readings of scintillometric measurements. The Miduk district, the center (caldera) of Kuh-e-Mosahim volcano, and Chenar granitoid massif are located in this zone [56].

The northern part of the studied area is subjected to hydrothermal copper and subordinate lead occurrences. The Lachah occurrence is of porphyry copper type, which includes Cu carbonates, chrysocolla, and limonite in the zone of superficial alterations together with primary pyrite and disseminated chalcopyrite. Cu mineralization of the vein type occurs at Chah Massi with pyrite, chalcopyrite, and galena as well as the Chehel Dokhraran area (quartz veins containing magnetite and malachite), where weak Cu disseminations also occurred. There is a hydrothermally altered zone with E-W trending on the southern slopes of Kuh-e-Masahim. A mineralized NNW-SSE fault zone is located in this part similar to the fault zone located in the south of the Kuh-e-sara. The Cu and Pb mineralizations are observed in these zones. The occurrences in the region are concerned with the Neogene volcanism [56].

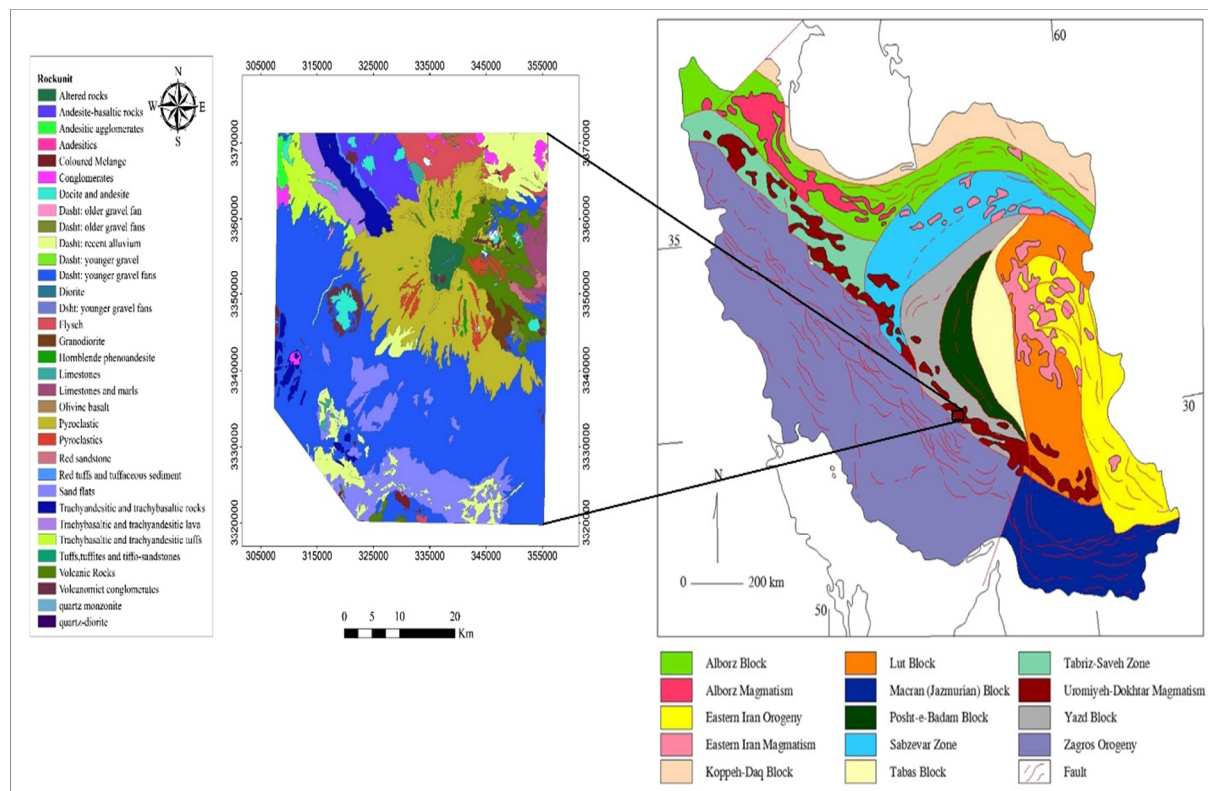


Figure 1. The Urumieh–Dokhtar volcanic belt and associated Cu occurrence in Iran, and simplified geological map of the studied area [57].

3. Geochemical dataset

Geochemical surveys play an important role in geoscience investigations in both the mineral exploration and environmental monitoring aspects. Field investigation includes photo-geological study, proper geochemical mapping by collecting samples, scintillometric measurements, and preparation of the collected samples at field base. The main goal of the photo-geological study is to design an optimum distribution of the samples and cover all catchment areas by an appropriate sampling grid size for the subsequent data processing using the KOMBI and PASIANS methods.

The density of the sampling is derived considering the morphological and geological features, and drainage pattern in the studied area. Projected sampling density (1 sample per 4 square kilometers in average) generally corresponds to the pre-Quaternary units, as shown in Figure 1. About 604 stream sediment samples of the -80 mesh (0.18 mm) fraction were collected in the studied area; the samples were analyzed for 44 elements by the ICP-MS method. Based on the mineralogical, geological, and geochemical results, it was found that the case study was suitable for the mineralization of Cu. A suggested method for exploration is to use the other elements involved in the host rock ore-forming process or developed in the host rocks at the time of ore formation, known as pathfinder elements. Therefore, the concentrations of Cu, As, Sb, Co, Mo, Sn, Ba, Zn, Pb, Cr, Ni, W, and B within these samples were considered since these elements represented the combination of mineralization in this area. The statistical results of these elements

are presented in Table 1. According to this table, concentrations of the elements represent high skewness values, which indicate the presence of the outliers within the data and their non-normal distribution. The quantile-quantile (Q-Q) plot is commonly used to determine the nature of data distribution (normal or log-normal) and recognize different geochemical populations [58]. The Q-Q plot of a uni-element data is applicable to define the population break points. The individual raw data is transformed logarithmically to explore whether the data is log-normally distributed. The Q-Q plots of the ln-transformed data (Figure 2) show that the majority of the values are distributed as log-normal functions, while a small number of high values follow a Pareto distribution. Therefore, the assumption of normal or log-normal distribution of the sample values is not effective in dealing with singular values. In fact, some of the values, especially extremely large ones, satisfy fractal or multi-fractal distributions. Hence, the distributed patterns of these geochemical data imply that the studied area has undergone multiple geological processes throughout the geological history, which leads to complex ore-forming processes [59, 60]. Therefore, it is appropriate to use the multi-fractal analysis to study the distribution of elements and assess the potential resources in this area. The extremely inhomogeneous distributions of Pb, Sb, and W are indicated regarding the larger coefficient of variation (CV) values for these elements. This means that the values for these elements are not widely dispersed, and high values are more likely to concentrate proximal to the ores.

Table 1. Statistical parameters of elements in stream sediment samples (raw values).

	Zn	Pb	Cr	Ni	Cu	As	Sb	Co	Sn	Ba	W	B	Mo
Number of samples	604.0	604.0	604.0	604.0	604.0	604.0	604.0	604.0	604.0	604.0	604.0	604.0	604.0
Mean	88.4	29.7	107.8	67.2	56.3	17.6	7.5	21.9	5.5	517.9	33.2	33.1	1.9
Median	71.0	14.0	87.5	57.0	43.0	15.0	4.0	18.0	5.0	513.5	6.0	28.0	2.0
Mode	48.0	8.0	70.0	22.0	32.0	15.0	1.0	10a	5.0	1200.0	6.0	2.0	2.0
Std. deviation	71.2	56.9	77.7	62.2	45.8	11.4	9.1	13.6	2.4	237.1	99.9	22.9	1.1
Variance	5071.5	3238.9	6043.8	3874.7	2093.2	129.4	82.8	185.6	5.5	56195.5	9989.4	526.0	1.2
Coefficient of variation	80.5	191.8	72.1	92.6	81.2	64.5	121.4	62.3	43.0	45.8	301.2	69.3	57.3
Skewness	4.7	7.4	2.1	8.2	3.3	6.6	3.1	1.3	6.6	0.6	5.0	1.6	3.5
Kurtosis	37.6	85.4	6.9	130.4	15.7	54.2	13.7	2.2	55.1	0.6	31.5	4.2	20.8
Range	912.0	868.0	602.0	1109.0	380.0	125.0	82.0	85.0	28.0	1125.0	994.0	163.0	11.0
Minimum	2.0	2.0	8.0	2.0	11.0	15.0	1.0	2.0	5.0	75.0	6.0	2.0	1.0
Maximum	914.0	870.0	610.0	1111.0	391.0	140.0	83.0	87.0	33.0	1200.0	1000.0	165.0	12.0
Percentiles													
5	28.0	5.0	29.3	9.0	19.0	15.0	1.0	7.0	5.0	144.3	6.0	2.0	1.0
25	51.0	9.0	55.0	30.0	31.0	15.0	1.0	12.0	5.0	356.5	6.0	17.0	1.0
50	71.0	14.0	87.5	57.0	43.0	15.0	4.0	18.0	5.0	513.5	6.0	28.0	2.0
75	104.0	23.0	134.0	91.0	63.8	15.0	10.0	28.8	5.0	651.0	6.0	44.0	2.0
95	189.5	127.8	254.0	158.8	137.8	33.0	25.8	48.8	9.5	927.5	244.5	76.8	4.0

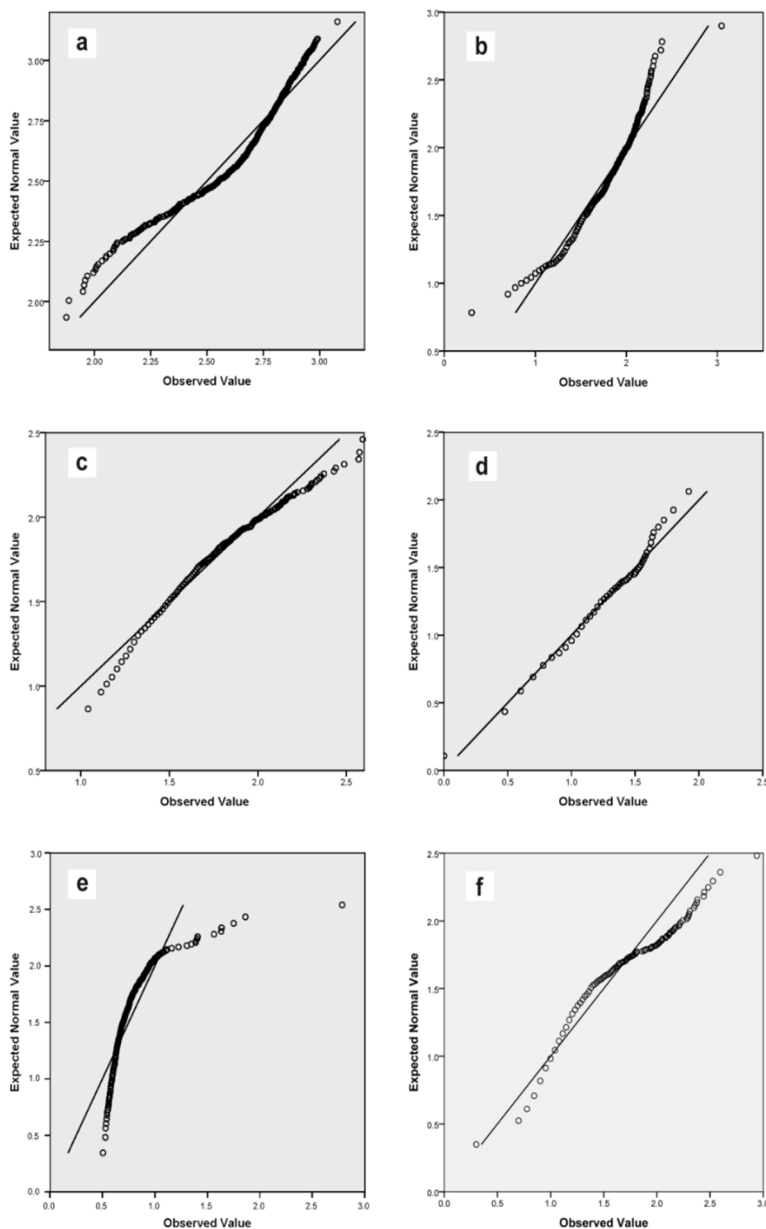


Figure 2. Q–Q plots of a) log Ba, b) log As, c) log Cu, d) log Sb, e) log Zn, and f) log Pb. The non-log normal distribution of the elemental concentrations are shown. The majority of the values distribute as a log-normal function, while a small number of high values follow a Pareto distribution.

4. Methods

In order to delineate the anomalies, the following geochemical processing methods were applied.

4.1. Factor analysis (FA)

According to the geological perspective, to obtain clues of existence of geological bodies, element relations are preferred over the single ones [61, 62]. In order to achieve the geochemical signatures of various element associations (i.e. integrated geochemical anomalies), correlation coefficient matrix based on FA is employed to integrate the singularity indices of geochemical

elements associated with the mineralization processes.

FA is one of the most popular methods of multivariate data analysis that has been proved as a powerful implement to visualize high-dimensional data in lower-dimensional spaces based on variance and covariance matrices. It is a practical tool to combine several correlated variables into a single one, and also reduce the dimensionality of datasets into uncorrelated principal components based on the covariance or correlation of variables that represent the inter-relationships among the multi-dimensional variables [19, 62].

A large set of geochemical variables are combined in few factors based on the method. The elemental concentration dataset is separated into several subsets, represented by different factors in FA. Factors are representative of the geological and mineralization processes that cause the correlation among these variables [61, 62].

There are four stages in FA: (i) Data is collected and a correlation matrix is estimated for the variables, (ii) Factors related to the correlation coefficients of the variables are extracted from the correlation matrix, (iii) Factors are rotated in order to maximize the relationship between the variables and factors, and (iv) Factors are scored to observe the position of the variables [63]. In this work, the Varimax rotation was employed to analyze the geochemical variables. A simple solution in Varimax means that each factor has a small number of large loadings and a large number of zero (or small) loadings. This fact simplifies the interpretation, as following a varimax rotation, each original variable tends to be associated with one (or a small number) of the factors, and every factor represents only a small number of variables. Formally, varimax finds a rotation of the original factors to maximize the variance of the loadings [63].

The classical approach for FA is to calculate the variability through the empirical variance. This approach is essentially based on computation of the eigenvalues and vectors of the sample covariance or correlation matrix. Therefore, its results are extremely sensitive to the presence of even a few atypical observations in the data. The outliers artificially increase the variance in an otherwise uninformative direction, which is determined as a principal component (PC) direction [62].

The eigenvectors do not represent the actual physical states properly since they are not aligned close to the local data clusters. Consequently, if the outliers are presented in the data, the classical FA results become unreliable [64]. Thus the rotated eigenvectors are of greater resemblance (with less variance) to the actual physical states than the un-rotated eigenvectors. The aim of FA is to achieve PCs that are not influenced by outliers through replacing the classic covariance matrix using reweighed minimum covariance determinant estimator [65].

In order to satisfy the decomposition, FA aims to seek coefficients $a_{kj}; j = 1, 2, \dots, p, p < m$, as in Eq. (1):

$$X_k^* = \sum_{j=1}^p a_{kj} f_j + g_k \quad (1)$$

where X_k^* is the normalized original variable with zero mean and unit standard deviation, and $k = 1, 2, \dots, m$, and f_1, f_2, \dots, f_p and g_1, g_2, \dots, g_p are the common and special factors, respectively [66]. Note that the common and special factors are independent; besides, the common factors are uncorrelated. If we assume n observations within each variable, the matrix form of Eq. (1) is as Eq. (2):

$$X = \Lambda F + g \quad (2)$$

where X is the input data, $m \times n$, Λ is the factor loading matrix, $m \times p$, and F is the common factor, $p \times n$ matrix [66].

Moreover, the geochemical data in the form of proportions such as weight percent and ppm are typically compositional, subjected to a constant sum (e.g. 100%, 1,000,000 ppm). The direct application of the multivariate statistical methods such as FA to raw D-parts compositional data leads to biased results, and consequently, misleading interpretations. For example, in order to obtain different results of correlation analysis, depending on whether the whole composition or only a sub-composition is considered, the problem of spurious correlations [67] occurs. Applying an appropriate transformation is crucial in implying FA to the compositional data. A log-transformation reduces data skewness but does not accommodate the compositional nature of the data. Aitchison (1986) has suggested several possible transformations from the family of log ratio transformations. In general, there are three popular log ratio transformation methods for opening the compositional data: additive log ratio transformation (alr) [67], centered log ratio transformation (clr) [59], and isometric log ratio transformation (ilr) [68], which, for a geochemical composition $X = (x_1, \dots, x_D)$ in the D-part simplex

$$S^D = \left\{ x = (x_1, \dots, x_D), x_i > 0, \sum_{i=1}^D x_i = k \right\}$$

(where k is an arbitrary positive constant), are expressed as Eqs. (3)-(5):

$$\text{alr} = (y_1, \dots, y_D) = \left(\ln \frac{x_1}{x_D}, \dots, \ln \frac{x_D}{x_D} \right) \quad (3)$$

$$crl = (y_1, \dots, y_D) = \left(\ln \frac{x_1}{\sqrt{\prod_{i=1}^D x_i}}, \dots, \ln \frac{x_D}{\sqrt{\prod_{i=1}^D x_i}} \right) \quad (4)$$

$$ilr = (y_1, \dots, y_D) = \sqrt{\frac{D-i}{D-i+1}} \log \frac{x_i}{\sqrt{\prod_{j=i+1}^D x_j}} \quad (5)$$

where y_1, \dots, y_D are the transformed values of geochemical variables x_1, \dots, x_D .

4.2. Power spectrum-area (S–A) multi-fractal method

The S–A multi-fractal method has been developed on the basis of the fractal concentration-area model and the frequency filtering technique [69]. Fractal filtering, as a developed technique to decompose a map or image into different components, helps to separate the anomaly from the background or extract other meaningful patterns from the geochemical map using both the frequency and spatial information [10]. Geochemical patterns in the spatial domain are considered as superimposed signals of different frequencies [40]. Based on this argument, Cheng et al. (1999) [70] have developed the idea of the C-A model into the frequency domain, and extended the S-A model to characterize the spectral energy density-area relationship.

These methods have been applied to determine filters in the frequency domain and separate regional and local variability in the geochemical data. These filters are used for reconstructing the anomaly and background patterns [46, 69, 70]. The advantage of dealing with fields in the frequency domain is that some complex convolution operations in the spatial domain for correlation analysis, filtering, and transformation are simplified significantly [10, 69].

According to the generalized scale invariance (GSI) viewpoint, this method has been expanded on the basis of the following power-law relationship between ‘area’, $A (\geq S)$, on the power spectrum plane with spectral values above a threshold S and the power spectrum S for fields with isotropic or generalized invariance scaling properties [70].

$$A (\geq S) \propto S^{-\beta} \quad (6)$$

Different values of β are estimated by plotting values of $\log A (\geq S)$ versus $\log S$ for various

ranges of S . The region of spatial wave numbers in the x and y directions giving different ranges of S with constant β are defined as filters.

As the filters created by S–A in the Fourier space maintain the anisotropy of the power spectrum with the identical scaling properties, patterns including distinct fractal properties and anisotropy are obtained in the spatial domain by means of the inverse Fourier transform regarding the applied filters.

The implication of this method includes plotting the values of contours and the areas enclosed by the contours on log-log paper. Straight-line segments are fitted to the values to construct power-law relations representing different self-similarities. The cut-off values obtained by intersecting these straight-line segments are applied to separate the contours into groups with similar shapes. The breakpoints separating these straight-line segments are regarded as cut-off values.

Filters are constructed on the basis of the contours separated in the Fourier frequency domain by means of the S–A method. The patterns are then converted into the spatial domain from the Fourier-transformed signals in the frequency domain providing decomposed patterns that reflect distinct underlying processes.

The inevitable influence of abrupt edge truncation on the S-A model is the main disadvantage of this method [71]. The edge effect is due to the irregular shape of the studied area as a result of the occurrence of high values at the edge points. Traditional solutions to reduce the edge effect are too smooth for the boundary of the image prior to applying the Fourier transformation. There are lots of smoothing methods such as Zero-padding [47]. This simple method partly reduces the edge effect; however, if the image remains distorted, it is inefficient. Moreover, due to the complexity of the geoscience data such as irregular shapes and holes within the missing data, the results of zero-padding methods are generally not persuasive. In geoscience image analysis, the decay functions are suggested to handle the edge effect [71]. As the decay functions do not reduce the edge effects for an irregular studied area, a further study can focus on reducing the edge effect for the S-A model [24].

In the recent years, many applications of the S-A method have been reported in the field of exploration geochemistry. Afzal et al. (2012) [72] have developed this method in a 3D dimension and applied it to detect the hypogene, supergene enrichment, leached, and barren zones. Recently,

Afzal et al. (2017) [73] have used the fractal-wavelet analysis to transform data from the spatial domain to the frequency domain.

4.3. Neural network adaptive wavelet (WNN)

Wavelet networks are traced back to the work done by Daugman (1988), in which Gabor wavelets have been used for image classification. Then these networks were developed by Zhang (2009). Wavelet networks are considered as a special feed-forward neural network [74-76].

WNN combines the wavelet theory and the feed-forward neural networks. It is considered as an alternative to the neural and radial basis function networks. This property is expressed as any function of $L^2(R)$, which is approximated to any given accuracy with a finite sum of the wavelets. Due to complication in interpretation of the model by neural networks, the wavelet has been recently used as an alternative of these networks [77]. On the other hand, training algorithms for WNN require a smaller number of iterations compared to neural network. For the approximation property and the convergence of the network, the choice of activation function is crucial. Transfer function calculates a layer output from its net input. In this work, the “pure line” function was applied as the output layer, and the types of wavelet functions used for the hidden layer were employed as the activation functions in WNN. In neural net, the activation function is constant, and functions cannot be changed or adjusted during the simulation. In other words, the activation function for WNN is adjusted by means of the dilation and translation parameters. The WNN parameters are dilation (d), translation (m), and weights (a, c), while the neural net parameters are weights and bias. The parameters are optimized by the gradient method with momentum for neural net and WNN [78].

4.3.1. Structure of WNN

In the recent years, due to the similarity between wavelet transform and one-hidden-layer neural network, the idea of integrating wavelets and neural net has been suggested. This has resulted in WNN. The wavelet theory provides effective guidelines for construction and initialization of the networks, and consequently, the training times are significantly decreased. Moreover, WNN provides a better performance by introducing two new parameters for the dilation (d) and translation (t) of wavelet transform [79]. The wavelet functions are classified into two categories: the orthogonal wavelets and the wavelet frames. As the

orthogonal wavelets cannot be expressed in closed form, the wavelet frames are employed in function approximation and process modeling [80]. Wavelet frames are constructed by a mother wavelet, which is a prototype for generating the other window functions. A wavelet $\phi_j(x)$ is derived from its $\phi(z_{jk})$ mother wavelet as Eq. (7):

$$\phi_j(x) = \prod_{k=1}^{N_i} \phi(z_{jk}) \quad z_{jk} = \frac{x - t_{jk}}{d_{jk}} \quad (7)$$

where N_i is the number of inputs. The network output y is calculated by Eq. (8):

$$y = \sum_{j=1}^{N_w} c_j \phi_j(x) + \sum_{k=1}^{N_i} a_k x_k \quad (8)$$

The WNN architecture is presented in Figure 3.

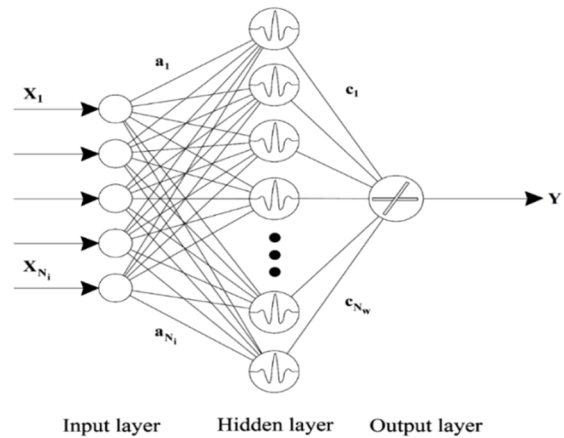


Figure 3. Structure of the WNN network composed of input layer, hidden layer with wavelet activation function, and output layer [81, 82].

Weights (a,c), translation (t), and dilation (d) are the adjustable parameters of WNN whose main aim is to update the parameters during the training phase; θ is the set of adjustable parameters as below:

$\theta = \{t_{jk}, d_{jk}, c_j, a_k\}$ and, $j=1, \dots, N_w, k=1, \dots, N_i$. The training is based upon the minimization. The quadratic cost function is used as shown in Eq. (9):

$$j(\theta) = \frac{1}{2} \sum (y_p - y)^{(2)} \quad (9)$$

In this equation, y is the network output, as shown in Eq. (8), and y_p is the process output. The minimization is performed by the iterative gradient basic methods. The partial derivative of the cost function with θ is calculated using Eq. (10):

$$\frac{\partial j}{\partial \theta} = -\sum e \frac{\partial y}{\partial \theta} \quad \text{and} \quad \theta = \{t_{jk}, d_{jk}, c_j, a_k\} \quad (10)$$

Eq. (11) has been used for updating the parameters.

$$\theta_{t+1} = \theta_t + \mu \left(-\frac{\partial j}{\partial \theta} \right) \quad (11)$$

where θ_t and θ_{t+1} are the figuration of parameters and updated parameters, respectively, and μ is the learning rate for Eq. (11). According to the above-mentioned reasoning based on the Scaled Conjugate Gradient (SCG) algorithm or Levenberg–Marquardt (L-M), the training algorithm can be summarized as the following steps:

- (a) Initialize the dilation and translation parameters according to the existing methods [81], and initialize node connection weights to random values. All these random values are limited in the interval (0, 1).
- (b) Input the learning samples and the corresponding output values to WNN.
- (c) The output values for the hidden neuron and output neuron are calculated using Eqs. (7) and (8), respectively.
- (d) Compute the instantaneous gradient vectors using Eq. (10).
- (e) The procedure of error back-propagation: parameters are adjusted using Eq. (11) to reduce the error, dilation, translation, and weights.
- (f) Returning to step (c), the process is continued until MSE satisfies the given error criteria.
- (g) If MSE satisfies the given error criteria, save the training parameters, and then the whole training of the WNN is completed; else, return to step (b). The whole training algorithm diagram is shown in Figure 4.

4.3.2. Initializations of Network Parameters

As an initial value affects the speed of the training and approximation to the global or local minimum, selecting the initial values of the network parameters is significant. Weight values are updated according to the derivative of the activation function at the stage of selecting the initial value. The functions and derivative of the functions cannot be equal to zero. For neural net, large values are not considered as the initial values for the parameters; otherwise, it will saturate, and the learning becomes slow. The initial values for the parameters are determined by means of the boundary input-output data and

feature of activation function for neural network. Initialization is more important for WNN as wavelets own the localization feature, and are out of the related domain due to the initial value. On the other hand, the initial values obtain the local wavelets and very small components of the gradient of the cost function [81]. Therefore, a random selection of the initial values for dilation (d_{jk}) and translation (t_{jk}) is not suitable for the process modeling. The center of wavelet j is initialized at the center of the parallelepiped defined by the N intervals $\{[p_k, q_k]\}$. For the k_{th} input dilation, a , and translation, b , correlations of the daughter wavelets are defined as Eqs. (12) and (13), respectively:

$$a_{jk} = 0.2(p_k - q_k) \quad (12)$$

$$b_{jk} = 0.5(p_k + q_k) \quad (13)$$

The initial extend of wavelets over the whole input domain is guaranteed by these initializations [81]. Figure 5 shows the plots of the mother wavelets accompanied by their daughters that are created by the mentioned procedure.

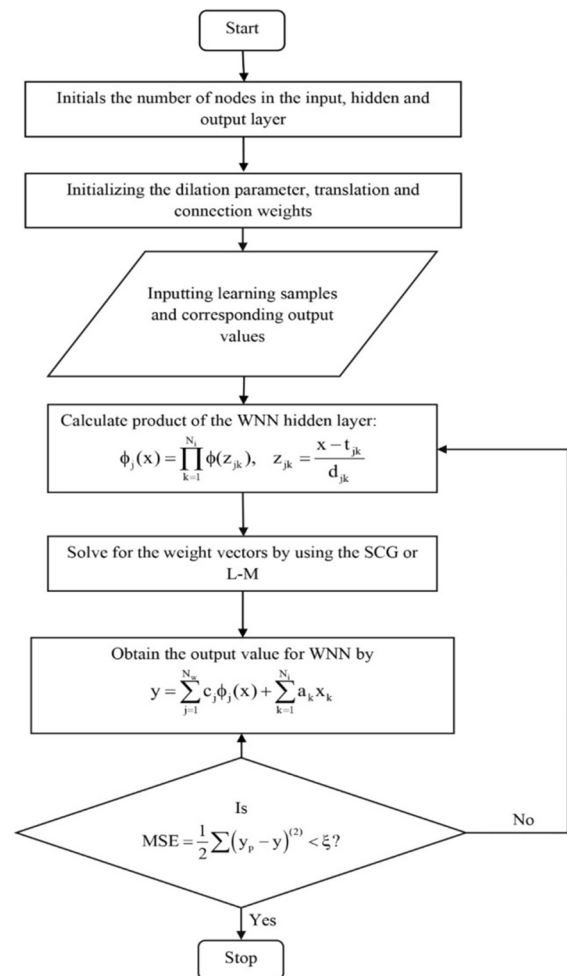


Figure 4. Learning algorithm for WNN [82].

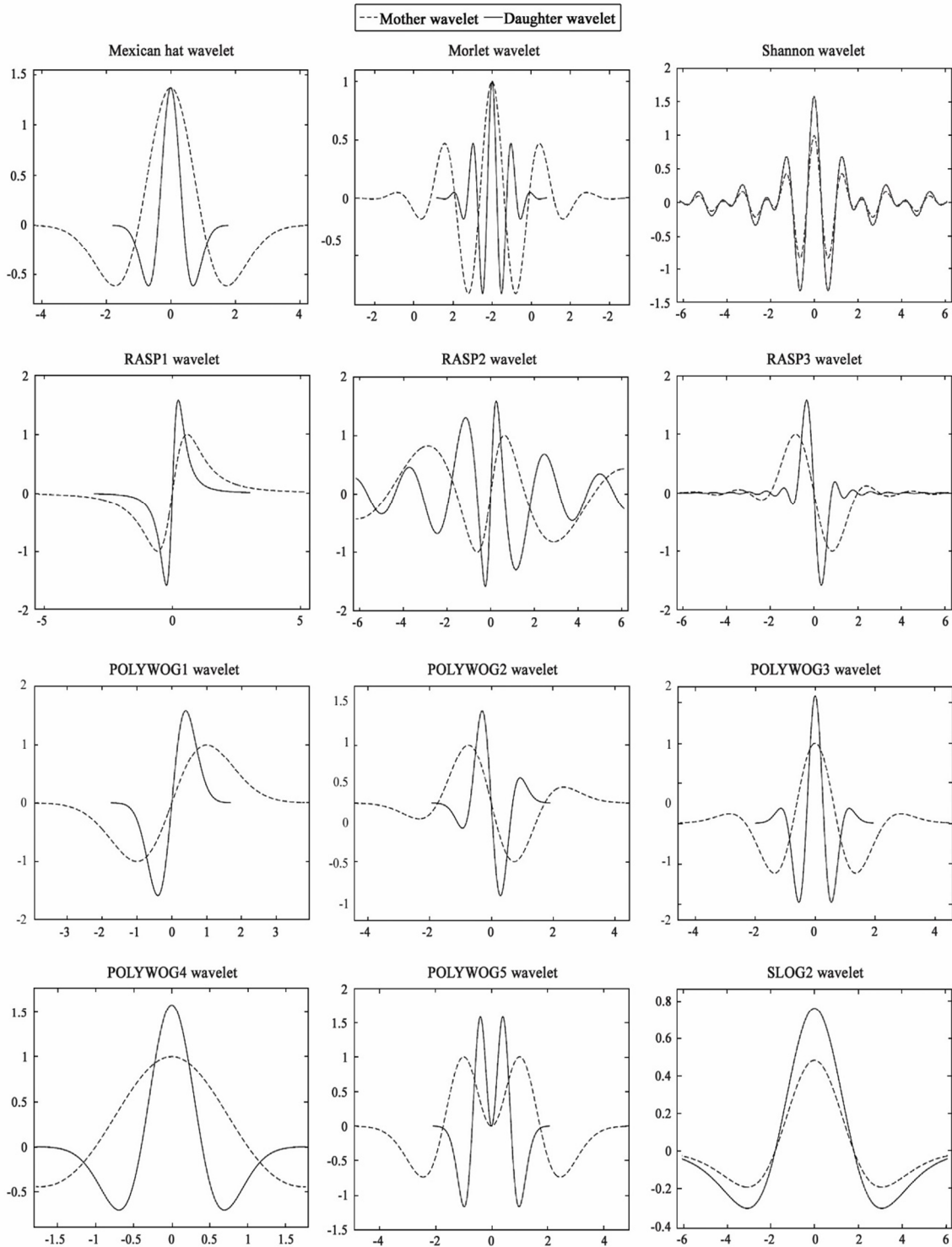


Figure 5. Different samples of mother wavelets with their daughters [82].

4.3.3. Stop conditions for training

Parameters of WNN are training during the learning phase of approximation. The desired function Scaled Conjugate Gradient and Levenberg–Marquardt methods are applied to adjustable parameters. Training is stopped when the variation in the gradient and parameters

reaches a lower bound or the number of iterations reaches a fixed maximum.

5. Result and discussion

5.1. Results of FA

The aim of the current work, which was performed on the stream sediment samples and assay data, was to evaluate FA in terms of the

Cu-related mineralization element associations. At First, the data for selected geochemical elements, i.e. Zn, Pb, Cr, Ni, Cu, As, Sb, Co, Sn, Ba, B, W, and Mo was transformed by ilr-transformation [59], which eliminated the effects of data closure. To explore the element associations, the results of FA with a varimax rotation for log transformed and ilr-transformed data were compared.

For each selected dataset with the corresponding eigenvalues greater than 1, five factors were determined. The results obtained for FA are presented in Tables 2 and 3. The biplot of Factor 1 (F1) versus Factor 2 (F2) for two selected dataset are presented in Figure 6. Biplot is a powerful tool to display the relationship between variables via loadings and observations via scores. It simultaneously visualizes the scores (data points or sample identifiers) and loadings (vectors) of FA. The correlation of variables was measured by the angle between any two vectors. Here, F1 and

F2 were accounted for 35.7% and 35.2% of the total variance of log transformed and ilr-transformed data, respectively. F1 of the log-transformed data (Figure 6a) consisted of positive loadings from most elements, except As, Sb, and W, while F1 of the ilr-transformed data (Figure 6b) included Zn, Sn, As, Ba, B, Cu, Ni, Mo, Pb, and Sb. The biplot showed that the loading area in positive quadrant of the plot was more concentrated in the log-transformed data than the ilr-transformed data. According to the previous studies on ore-forming element correlations in metallogenic processes for various Cu deposits based on ore samples in the Miduk ore district [83], Cu element is often correlated with Cu, As, Mo, Sb, Zn, and Pb. The results obtained show that the factors obtained by FA of the ilr-transformed data are more meaningful in the context of regional mineralization in the region.

Table 2. Loadings of FA carried out using log-transformed data.

Element	Factor 1	Factor 2	Factor 3	Factor 4	Factor 5
Zn	0.053	-0.172	0.763	-0.003	-0.278
Pb	0.109	0.281	0.802	0.142	0.140
Cr	0.658	0.477	0.276	-0.182	-0.102
Ni	0.873	-0.102	0.118	0.059	-0.011
Cu	0.478	0.117	0.598	0.173	.336
As	-0.004	0.334	-0.047	0.696	-0.340
Sb	-0.059	0.579	0.311	-0.183	-0.053
Co	0.828	-0.061	-0.094	0.085	-0.031
Sn	0.175	-0.643	0.222	-0.035	-0.129
Ba	0.023	0.802	0.087	0.124	0.084
W	-0.096	0.110	-0.033	-0.016	0.841
B	0.729	-0.129	0.156	0.013	-0.056
Mo	0.089	-0.201	0.198	0.723	0.190

Table 3. Loadings of FA carried out using ilr-transformed data.

Element	Factor 1	Factor 2	Factor 3	Factor 4	Factor 5
Zn	0.870	0.042	-0.175	-0.011	0.107
Pb	0.894	0.099	0.102	0.060	0.038
Cr	-0.029	0.641	0.449	-0.317	-0.022
Ni	0.054	0.753	-0.088	0.079	-0.036
Cu	0.681	0.266	0.177	0.282	-0.200
As	0.366	-0.250	0.375	0.375	0.590
Sb	0.290	0.184	0.328	-0.425	0.059
Co	-0.033	0.777	0.009	0.058	0.022
Sn	0.016	0.234	-0.653	0.033	0.139
Ba	0.175	-0.643	0.783	0.010	0.096
W	-0.106	-0.190	0.136	0.152	-0.783
B	0.012	-0.723	-0.239	0.083	0.150
Mo	0.188	0.117	0.005	0.767	-0.018

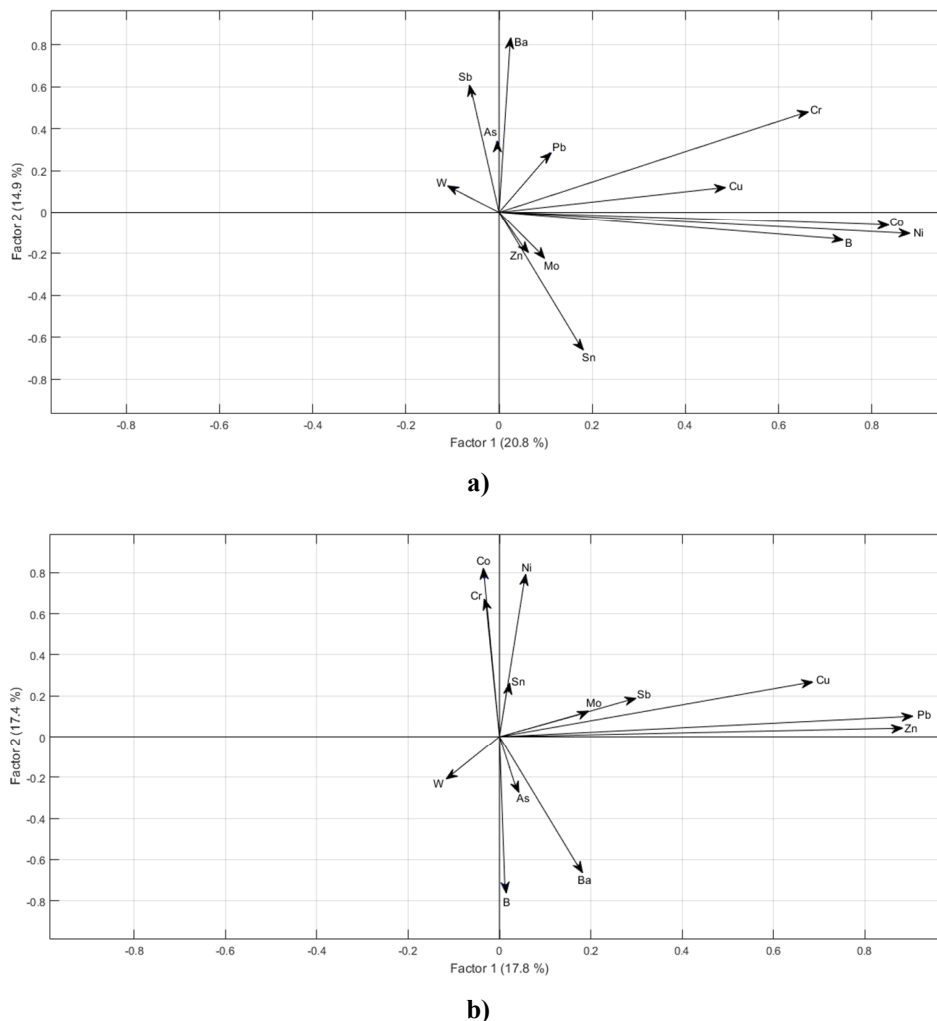


Figure 6. a) Plots of Factor 1 loadings versus Factor 2 loadings of the log-transformed data, and b) ilr-transformed data. The arrows represent the original elements. The direction of the arrows indicates the relative loadings of the variable. The angle between any two arrows is a measure of the correlation between the variables.

5.2. Results of S–A

The spatial distribution of Factor 1 obtained for the Inverse Distance Weighted (IDW) method through ArcGIS shows a mixed and complicated pattern (Figure 7). The patterns for F1, as shown in Figure 7, represent the total analyzed values in the stream sediment samples. These values are caused by overlapping processes such as sedimentation, volcanic activity, igneous activity, faulting, and mineralization. Due to the different natures of the mentioned processes, the related patterns treated as space series are distinguishable according to various properties such as frequency distribution. Distinctive frequency distribution and scaling property allow the S-A fractal filtering technique to separate the patterns according to the distinct self-similarity observed in the spatial patterns of the frequency domain. The Spectrum-Area (S-A) technique is used to decompose the mentioned mixed pattern. At First,

the F1 map is taken into the frequency domain by means of the 2D Fourier transformation.

Two components, the power spectrum density and phases, are obtained. The spectrum energy density (S) and the area (A) are enclosed by the values greater than or equal to the threshold for F1, plotted on a log-log scale (Figure 8). The S-A method ensures that the power spectrum value (S) and the area (A), as shown by the fitted straight-line segments on the log-log axes, follow the power law relationships. Variant straight-line segments with different slopes represent various self-similarities, which correspond to different patterns in the spatial domain. For example, for Factor 1, four straight lines are fitted by means of the Least Squares (LS) method. This results in four ranges of power energy spectrum (S) that maintain distinct scaling properties of the S-A relation. In the case of Factor 1, the $\text{Log } S_0 = 5.1423$, $\text{Log } S_1 = 6.3727$, and

Log $S_2 = 6.8786$ values define three thresholds. $S < S_2$ represents anomalies and the power spectrum, while $S > S_0$ corresponds to the background [70].

Furthermore, three types of fractal filters are constructed based on the log S–log A plot: low pass, high-pass, and band-pass spectral energy density filters. The length of the intersection points, as threshold S_0 or S_1 , is defined by two intersecting lines on both sides of the two segments. The various slope of the segments indicates that they meet different fractal characteristics. Based on the log S–log A plot, three types of fractal filters can be defined, as follow:

$$G_A(\omega) = \begin{cases} 1 & S(\omega) \leq S_0 \\ 0 & S(\omega) > S_0 \end{cases} \quad (14)$$

$$G_B(\omega) = \begin{cases} 1 & S(\omega) \leq S_2 \\ 0 & S(\omega) < S_2 \end{cases} \quad (15)$$

$$G_C(\omega) = \begin{cases} 1 & S_2 \leq S(\omega) \leq S_0 \\ 0 & \text{otherwise} \end{cases} \quad (16)$$

The investigations indicate that the spectral energy density is inversely related to the spectral frequency. It has also been proved that if $G_A(\omega)$ of

the spectral energy density is less than $G_B(\omega)$, the wave number of $G_A(\omega)$ is larger than $G_B(\omega)$. Accordingly, $G_A(\omega)$ and $G_B(\omega)$ correspond to high and low frequencies, respectively. Therefore, $G_A(\omega)$ can be used as the high-frequency energy spectral density filter, and $G_B(\omega)$ is the low-frequency energy spectral density filter. $G_A(\omega)$ and $G_B(\omega)$ are considered as the anomaly and background filters, respectively. $G_C(\omega)$ is used to strain out energy spectra less than S_0 and greater than S_2 , and retains the spectral components within the interval (S_2, S_0) . Therefore, $G_C(\omega)$ is a band-pass filter in a specific interval.

The resulting S-A model is influenced inevitably and severely by abrupt edge truncation. The edge effect due to the irregular shape of the studied area results in high values occurring at the edge of the studied area. The edge effect has to be removed in the irregular-shaped area of our work. In Figure 9, the edge effect for F1 is effectively addressed. There are various solutions to eliminate the edge effect [24, 71, 83], though the zero-padding approach is applied in this paper. Zero-padding is one of the most frequently used smoothing methods that partly reduces the edge effect.

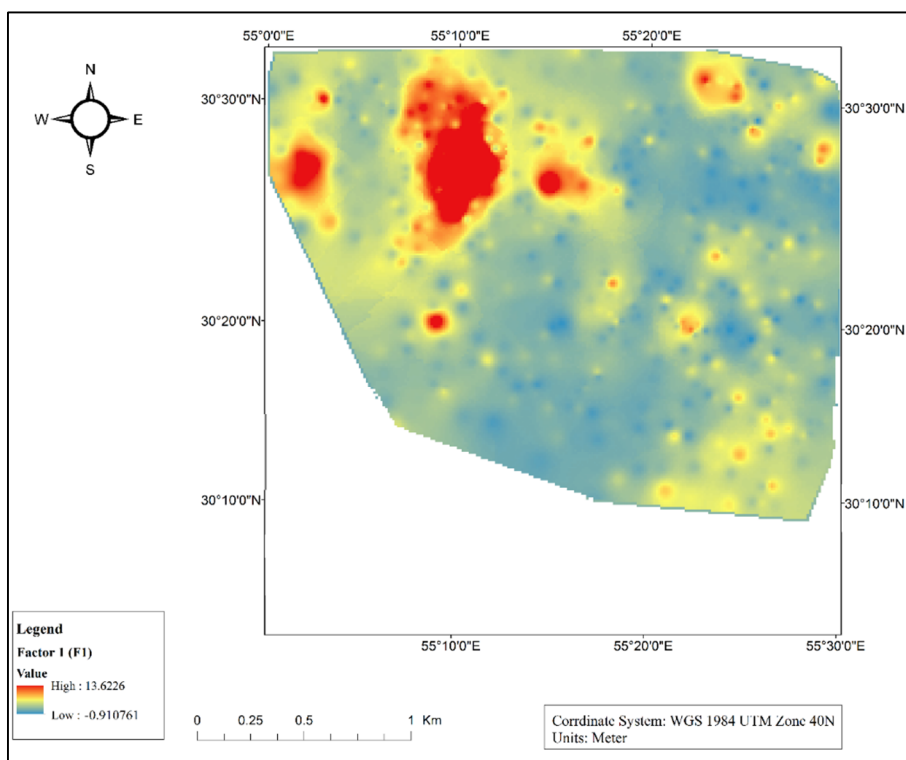


Figure 7. The geochemical map created by F1 using ilr-transformed stream sediment data (values are presented in ppm scale).

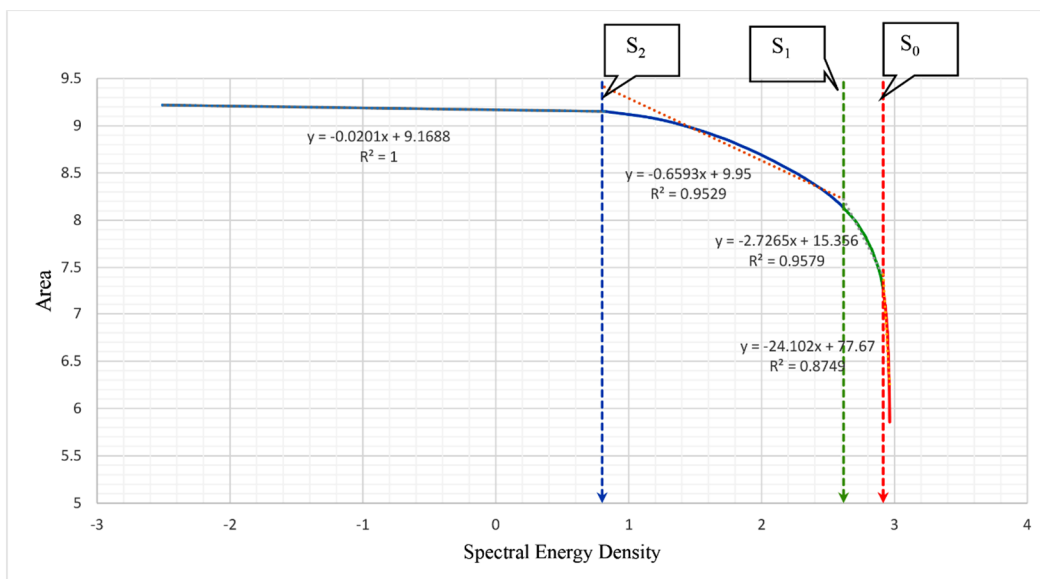


Figure 8. A log-log plot showing the relationship between spectral energy density (S) and area (A) of factor 1. The vertical axis represents area and the horizontal axis is the spectral energy density. Straight lines are fitted by means of the Least Squares (LS) method. Three breakpoints are indicated by $S_0 = 2.91$, $S_1 = 2.61$, and $S_2 = 0.8$.

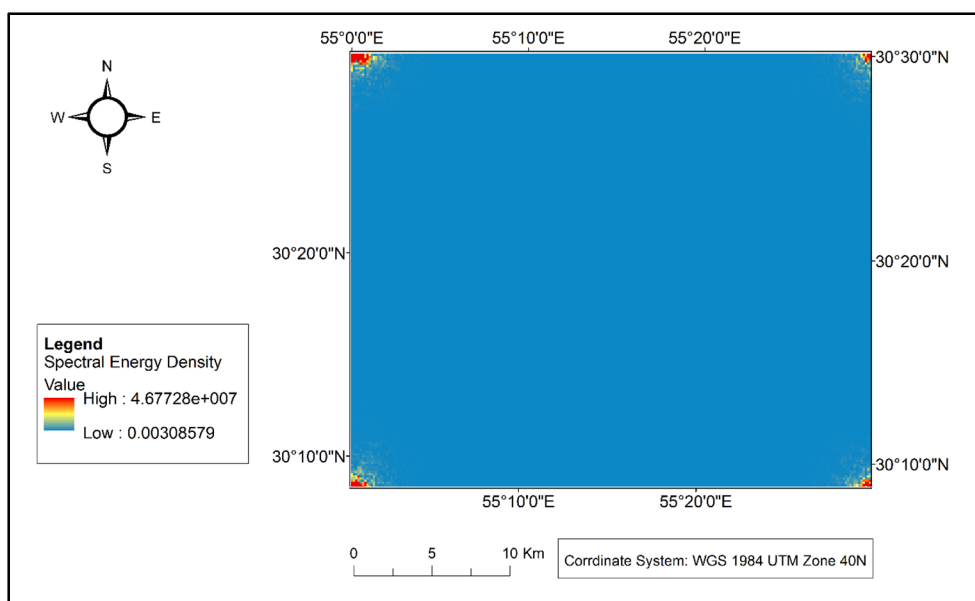


Figure 9. The edge effect of Factor 1.

High-frequency, low-frequency, and band pass filters are applied to the Fourier-transformed results after removing the edge effect and determining the thresholds. Then the inverse Fourier transform is implied to bring back the data to the spatial domain and plot the anomaly and the background map. The F1 anomaly and background maps obtained using the inverse Fourier transformation are shown in Figure 10. The promising areas of Cu mineralization are located in the places with high background and anomaly values. Also the high positive values are mainly within the areas related to a high geochemical background value, which indicates

that the occurrence of the anomalies in high background areas is identifiable.

Considering the high values of the anomaly and background maps, the potential mineralization areas are mostly located at the NW section over trachybasaltic and trachyandesitic lithological unit, which shows a strong phyllic alteration associated with Cu mineralization. The results obtained show that S–A, based on distinct anisotropic scaling properties, is a useful tool to identify the geochemical anomalies because it considers the spatial characteristics of the geochemical variables.

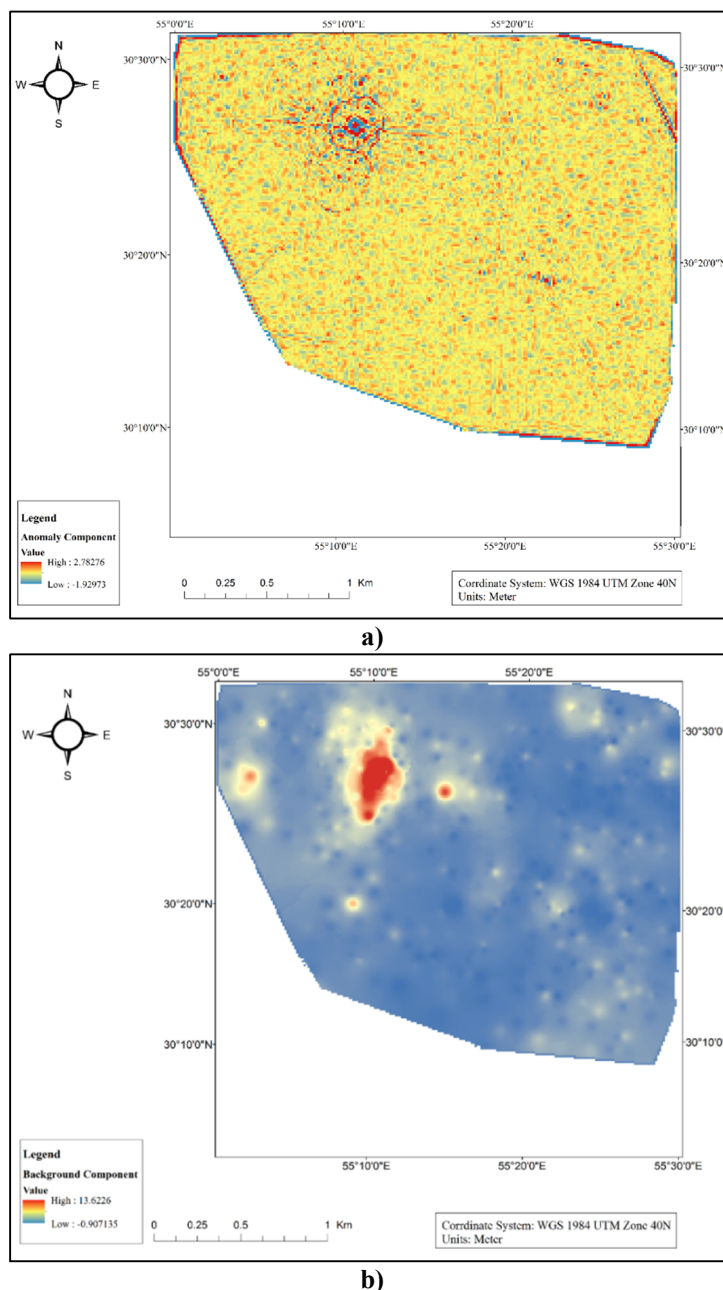


Figure 10. a) Anomaly and b) background maps showing promising areas of F1 using the S-A fractal model.

5.3. Results of WNN

WNN is applied in Cu mineralization in the studied area based on the stream sediment samples. A supervised Wavelet Neural Network (or WNN) method is used, which consists of the following steps:

5.3.1. Data preparation

Geochemical components associated with Cu mineralization (Factor 1) that consist of Cu, As, Sb, Zn, and Pb are used as the input data. At the beginning of the modeling process, the data is normalized, which helps to scale the input data and output, and consequently, leads to a more efficient prediction. Scaling the input data and

output prior to imply ANN is very significant. The main advantage of the scaling process is to avoid the domination of the attributes in greater numeric ranges to those in the smaller ranges as well as to avoid numerical difficulties during the calculation [84, 85]. In order to normalize the data, different methods have been developed to improve the network training. Such methods include “the normalized data that is in the range of [-1 1] using the maximum and minimum dataset”, “the normalized data using the mean and standard deviation of the dataset”, and finally, “the normalized data in the range of [01] using the Eq. (17)”:

$$X_{norm} = \frac{x - x_{min}}{x_{max} - x_{min}} \quad (17)$$

where X_{norm} is the normalized data that is transformed, x is the normalized input data, and x_{max} and x_{min} are the maximum and minimum values of the original data, respectively [86]. In this work, the input data and the output are normalized by the mentioned formula.

If the division is not considered properly, the results might be inaccurate and illogical. The wavelet neural network data falls into three categories: 1) The training data, which is definite

and clear, and is used during the training process, 2) The testing data, which is used after the training process while their target is not clear, and 3) The validation data, which is used during the training process to avoid over-fitting, while it is not definite. In this work, all the available datasets were divided randomly into three distinct subsets consisting of the training, validation, and testing data.

The proportions of each subset were 70%, 15%, and 15% of the whole data (Table 4). The spatial distribution of the extracted samples is shown in Figure 11.

Table 4. Range of different parameters for training, testing, and validating datasets.

Effective parameters	Train data (422 samples)			Test data (91 samples)			Validation data (91 samples)			
	Min	Average	Max	Min	Average	Max	Min	Average	Max	
Parameter	Cu	13	55.66	391	16	60.95	371	11	54.93	227
	As	15	17.37	91	15	19.52	140	15	16.87	82
	Sb	1	7.30	63	1	8.70	83	1	7.19	44
	Zn	11	87.31	545	2	99.85	914	12	82.26	234
	Pb	2	27.44	395	2	41.86	870	2	27.81	204

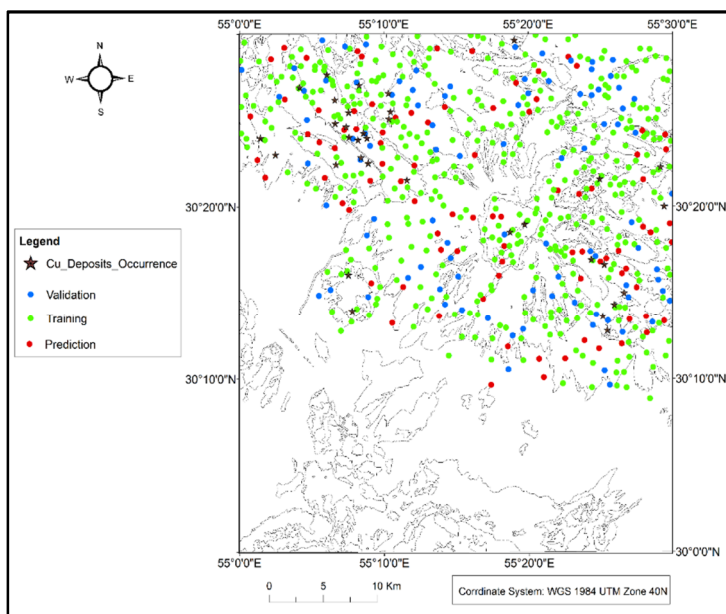


Figure 11. Spatial distribution of the selected samples for WNN modeling.

There are different error metrics to evaluate the accuracy of the models including coefficient of determination (R^2), EI, RMSE, and mean bias error (MBE). In addition to these indices, persistence index (PI) and extrapolation index (EXI) are also included [87, 88]. All the selected indices (except MBE and R^2) and various error metrics for evaluating the hydrograph have been explained by Crochemore et al. (2015). R^2 and RMSE are used in this work as the error metrics. R^2 measures the degree of correlation between the observed and predicted values. A model strength

is measured by R^2 through developing a relationship among the input and output variables. The R^2 values range from 0 to 1, 1 indicating a perfect fit between the data and the line drawn through them, and 0 representing no statistical correlation between the data and the line. R^2 is calculated by [89]:

$$R^2 = 1 - \frac{\sum_{k=1}^N (t_k - y_k)^2}{\sum_{k=1}^N (t_k - \bar{t}_k)^2} \quad (18)$$

where t_k and y_k are the target and network outputs for the k_{th} output, respectively; \bar{t}_k is the average of the targets; and N is the total number of the considered events.

RMSE indicates the discrepancy between the observed and calculated values. The lower the RMSE, the more accurate is the prediction. RMSE is calculated by [89]:

$$RMSE = \sqrt{\frac{\sum_{i=1}^N (y_i - \bar{y}_i)^2}{N}} \quad (19)$$

where y_i is the observed data, \bar{y}_i is the calculated data, and n is the number of observations. RMSE is equal to 0 for a perfect fit between the observed and forecasted values. R^2 and RMSE for the best fit between the observed and calculated values,

which is unlikely to occur, are equal to 1 and 0, respectively [90].

5.4. Modeling

In the standard feed-forward neural networks, the activation function of hidden layer neurons is a sigmoid function. In order to increase the generality of performance, the activation functions are substituted with different daughter wavelet functions. This creates various WNNs; note that the WNN model is implemented using MATLAB. Different wavelet function formulas as activation functions are shown in Table 5. The results of the observed and predicted data obtained from the neural network adaptive wavelet (WNN) model are summarized in Table 6. Types of WNN architectures with initialization dilation and translation parameters are shown in Table 7.

Table 5. Proposed wavelets for application in WNN.

Case number	Name	$h(\tau)$	$\partial h/\partial b$
1	Morlet	$\cos(\omega_0 \tau) \exp(-0.5 \tau^2)$	$\frac{1}{a} [\omega_0 \sin(\omega_0 \tau) \exp(-0.5 \tau^2) + \tau h(\tau)]$
2	Mexican hat	$(\tau^2 - 1) \exp(-\frac{\tau^2}{2})$	$(3\tau - \tau^3) \exp(-\frac{\tau^2}{2})$
3	RASP1	$\frac{\tau}{(\tau^2 + 1)^2}$	$\frac{1}{a} \frac{(3\tau^2 - 1)}{(\tau^2 + 1)^3}$
4	RASP2	$\frac{\tau \cos \tau}{\tau^2 + 1}$	$\frac{\tau(\frac{\tau^2 + 1}{a} \sin(\tau) + (\frac{\tau^2 - 1}{a}) \cos(\tau))}{(\tau^2 + 1)^2}$
5	RASP3	$\frac{\sin(\pi\tau)}{\tau^2 - 1}$	$\frac{(\frac{2\tau}{a} \sin(\pi\tau) - \pi(\frac{\tau^2 - 1}{a}) \cos(\pi\tau))}{(\tau^2 - 1)^2}$
6	SLOG1	$\frac{1}{1 + e^{-\tau+2}} - \frac{1}{1 + e^{-\tau+3}} - \frac{1}{1 + e^{-\tau-3}} + \frac{1}{1 + e^{-\tau-1}}$	$\frac{1}{a} [-\frac{e^{-\tau+1}}{(1 + e^{-\tau+1})^2} - \frac{e^{-\tau+3}}{(1 + e^{-\tau+3})^2} - \frac{e^{-\tau-3}}{(1 + e^{-\tau-3})^2} + \frac{e^{-\tau-1}}{(1 + e^{-\tau-1})^2}]$
7	SLOG2	$\frac{3}{1 + e^{-\tau-1}} - \frac{3}{1 + e^{-\tau+1}} - \frac{1}{1 + e^{-\tau-3}} + \frac{1}{1 + e^{-\tau+3}}$	$\frac{1}{a} [-\frac{3e^{-\tau-1}}{(1 + e^{-\tau-1})^2} - \frac{3e^{-\tau+1}}{(1 + e^{-\tau+1})^2} - \frac{e^{-\tau-3}}{(1 + e^{-\tau-3})^2} + \frac{e^{-\tau+3}}{(1 + e^{-\tau+3})^2}]$
8	POLYW OG1	$\tau \exp(-\frac{\tau^2}{2})$	$\frac{1}{a} (\tau^2 - 1) \exp(-\frac{\tau^2}{2})$
9	POLYW OG2	$(\tau^3 - 3\tau) \exp(-\frac{\tau^2}{2})$	$\frac{1}{a} (\tau^4 - 6\tau^2 + 3) \exp(-\frac{\tau^2}{2})$
10	POLYW OG3	$(\tau^4 - 6\tau^2 + 3) \exp(-\frac{\tau^2}{2})$	$\frac{1}{a} (\tau^5 - 10\tau^3 + 15\tau) \exp(-\frac{\tau^2}{2})$
11	POLYW OG4	$(1 - \tau^2) \exp(-\frac{\tau^2}{2})$	$\frac{1}{a} (3\tau - \tau^3) \exp(-\frac{\tau^2}{2})$
12	POLYW OG5	$(3\tau^2 - \tau^4) \exp(-\frac{\tau^2}{2})$	$\frac{1}{a} (-\tau^5 + 7\tau^3 - 6\tau) \exp(-\frac{\tau^2}{2})$
13	Shannon	$\frac{\sin 2\pi\tau - \sin \pi\tau}{\pi\tau}$	$\frac{\pi}{a} \frac{(-\pi\tau \cos \pi\tau - 2\pi \cos \pi\tau + \sin \pi\tau - \sin 2\pi\tau)}{(\pi\tau)^2}$

Table 6. Results of observed and predicted data obtained from WNN. The best obtained network is in bold.

Number	Wavelet name	Number of neurons	RMSE			SSE			Determination coefficient (R ²)		
			train	test	validation	train	test	validation	train	test	validation
1	Shannon	12	0.37	0.41	0.31	1.44	1.69	1.48	0.88	0.81	0.86
2	Mexican hat	12	0.33	0.46	0.35	1.33	1.63	1.37	0.89	0.84	0.87
3	Morlet	12	0.22	0.35	0.26	1.12	1.43	1.24	0.96	0.90	0.92
4	POLYWOG1	12	0.28	0.38	0.32	1.22	1.52	1.36	0.93	0.89	0.91
5	POLWOG2	12	0.26	0.45	0.37	1.26	1.53	1.31	0.92	0.88	0.90
6	POLYWOG3	12	0.24	0.41	0.33	1.26	1.58	1.35	0.92	0.88	0.90
7	POLYWOG4	12	0.27	0.44	0.33	1.26	1.63	1.55	0.92	0.88	0.90
8	POLYYOG5	12	0.28	0.48	0.36	1.29	1.58	1.63	0.91	0.86	0.88
9	SLOG1	12	0.24	0.41	0.37	1.22	1.65	1.32	0.93	0.89	0.90
10	SLOG2	12	0.27	0.37	0.34	1.22	1.55	1.42	0.93	0.89	0.90
11	RASP1	12	0.29	0.42	0.33	1.29	1.65	1.57	0.91	0.86	0.88
12	RASP3	12	0.28	0.47	0.31	1.29	1.63	1.63	0.91	0.86	0.88

Table 7. Different types of WNN architectures with initialization dilation and translation parameters.

Wavelet name	Structure	Dilation	Translation
Shannon	5-12-2	0.2	5
Mexican hat	5-12-2	0.3	14
Morlet	5-12-2	2	10
POLYWOG1	5-12-2	10	20
POLWOG3	5-12-2	5	10
RASP1	5-12-2	5	20
SLOG1	5-12-2	2	20

In this work, the number of hidden layers and neurons were selected by repeated trials and estimated errors. As shown in Table 6, the optimal results were obtained when one hidden layer with 12 neurons with the Morlet activation function was used for the training. Some of the inputted neurons correspond to the five inputted Cu mineralization indicator elements.

Two neurons of the output layer correspond to the Cu deposits and the non-deposits, which are

assigned as (1, 0). The architecture of the WNN model is shown in Figure 12. WNN was used to predict the test points after combination with the architecture and the saved weights as well as evaluating with the validation data. The results obtained show that all points agree with the expected value, while indicating a high classification accuracy. The predicted results (Figure 13) are in good agreement with the S-A model results.

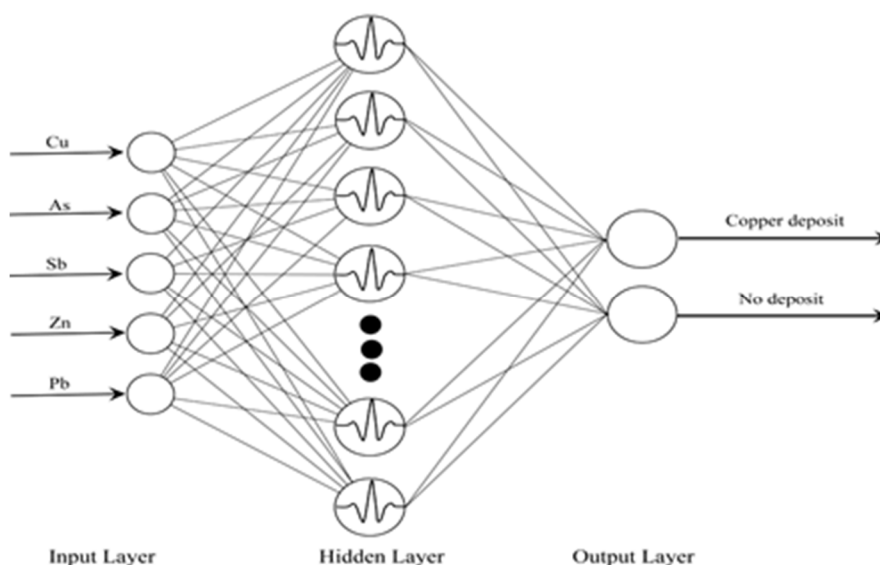


Figure 12. Wavelet neural network (WNN) model for Cu mineralization prediction.

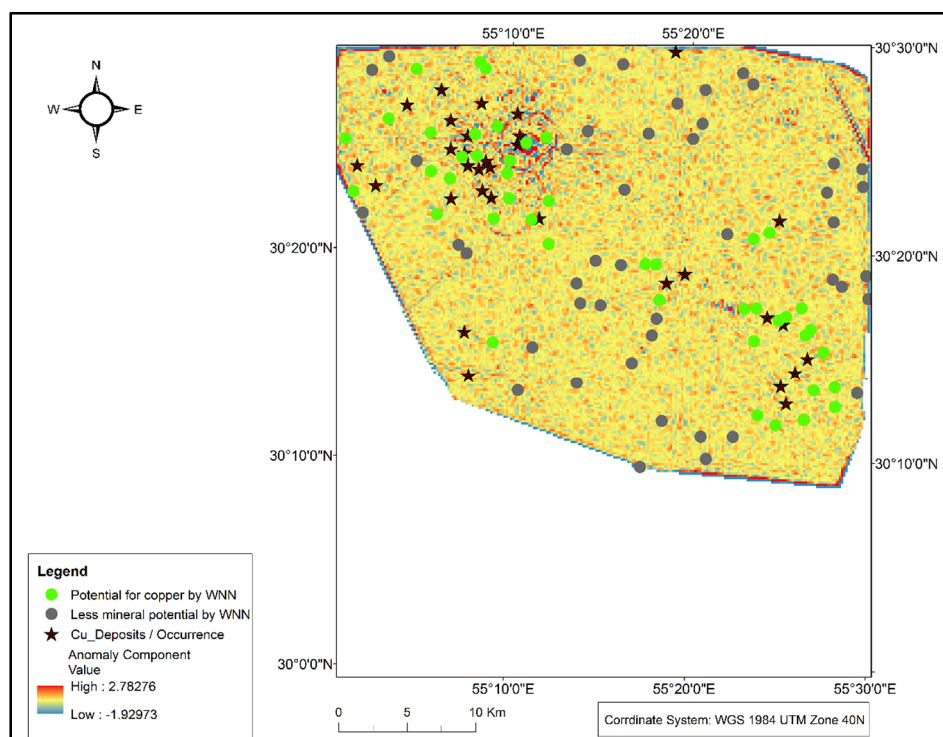


Figure 13. Integrated map of Cu potential evaluation by means of S-A and WNN methods.

The results obtained for the WNN and S-A multi-fractal were compared and correlated to specific geological particulars of the region, while considering the nature of lithological units, faults, and alteration. Cu distribution in the Shahr-e-babak, the faults, and the alteration areas, are in good agreement with the results of the S-A and WNN models. The anomalous parts clearly indicate the main identified faults, especially in the northwestern (Miduk) side of the area that is comfortable with the existing structural settings and controls. Comparison between tectonics confirms the forces creating the regional stress field, while Cu anomalies show that faults that intersect the anomalies are situated near those structures. On the other hand, faults and elemental anomalies are in a proportional relationship. High grade elemental anomalies occurred inside and within the fault zones or located at faults intersection areas. It can be deduced that the fault density has a direct positive correlation with mineralization, especially in the northwestern parts of the studied area [91, 92].

6. Conclusions

The decomposition of the mixed geochemical patterns is a challenge in prospecting mineral resources and environmental assessment. The Shahr-e-Babak district is a Cu mineralization prospective area that has a complicated geochemical surface and complex tectonic setting.

Due to the importance of geochemical mapping in minimizing the cost and time of prospecting as well as maximizing prospecting benefit of a mineral exploration program, and also decreasing the uncertainty caused by the unknown/complex geochemical variables, a geochemist and exploration geologist has to be able to apply a powerful, transparent, and robust method to separate the anomaly from the background. In this work, the FA and (S-A) fractal models, with the aid of the wavelet neural network (WNN) were applied to separate the mixed geochemical anomalies associated with the Cu-mineralization. The results obtained indicate that:

(1) Due to the effects of the compositional data closure, the geochemical data has to be initially opened before being analyzed. This is because the data closure problem results in spurious correlations or associations between the geochemical variables, and accordingly, complicates the interpretation of the various correlations between the same variables from different sub-compositions;

(2) The hybrid method combining the FA and S-A fractal models is an efficient tool for identifying the geochemical anomalies. The former is used to integrate the multi-element concentration values associated with the Cu-mineralization information, and the latter is used to decompose the mixed geochemical patterns in a complex geological setting. The S-A

multi-fractal model, which is based upon self-similarity and self-affinity, addresses the spatial characteristics of the geochemical patterns and reduces the geochemical noise and helps to identify weak geochemical anomalies;

(3) WNN is used for a more particular knowledge of the non-linear relationships between the geochemical variables and mineral resources. The results obtained show that the predicted points are in a good agreement with the S-A model results;

(4) In this work, the wavelet neural network was used as an alternative to the artificial neural networks. The WNN networks were used for function approximation in static and dynamic non-linear input-output modelling of processes. WNN improves the performance of the trained network in aspects of fast convergence and robustness to noise interference. It also consists of a highly complex ability to learn and track the unknown/undefined complicated systems. The results obtained showed that the WNN network with Morlet transfer function obtained the best result to examine the non-linear relationships between the geochemical variables and mineral resources;

(5) The results obtained from this work indicate that there are potential areas for the discovery of new mineral deposits. The favorable areas are in the NW of the studied area and partly in the NE side, which is comfortable with the existing structural settings and controls;

(6) The results obtained show that the hybrid method, as a robust approach, is a more accurate alternative than the existing methodologies for identifying the geochemical anomalies. Therefore, it is suggested to be applied for geochemical mapping in similar problems, especially in polymetallic districts with a complex geologic and tectonic setting.

References

[1]. Carranza, E.J.M., Zuo, R. and Cheng, Q. (2012). Fractal/multifractal modelling of geochemical exploration data. *Journal of Geochemical Exploration*. 122: 1-3.

[2]. Zuo, R. and Wang, J. (2016). Fractal/multifractal modeling of geochemical data: a review. *J Geochem Explor*. 164: 33-41.

[3]. Cheng, Q. (2008). Modeling local scaling properties for multiscale mapping. *Vadose Zone J*. 7: 525-532.

[4]. Deng, J., Wang, Q., Yang, L., Wang, Y., Gong, Q. and Liu, H. (2010). Delineation and explanation of geochemical anomalies using fractal models in the

Heqing area, Yunnan Province, China. *J Geochem Explor*. 105: 95-105.

[5]. Chen, Y., Zhao, P., Chen, J. and Liu, J. (2001). Application of the geo-anomaly unit concept in quantitative delineation and assessment of gold ore targets in Western Shandong Uplift Terrain, Eastern China. *Nat. Resour. Res*. 10: 35-49.

[6]. Singer, D.A. and Kouza, R. (2001). Some simple guides to finding useful information in exploration geochemical data. *Nat. Resour. Res*. 10: 137-147.

[7]. Wang, W., Zhao, J. and Cheng, Q. (2011). Analysis and integration of geo-information to identify granitic intrusions as exploration targets in southeastern Yunnan District, China. *Comput Geosci*. 37: 1946-1957.

[8]. Yuan, F., Li, X., Zhou, T., Deng, Y., Zhang, D. and Xu, C. (2015). Multifractal modelling-based mapping and identification of geochemical anomalies associated with Cu and Au mineralisation in the NW Junggar area of northern Xinjiang Province, China. *J Geochem Explor*. 154: 252-264.

[9]. Li, C., Ma, T. and Shi, J. (2003). Application of a fractal method relating concentrations and distances for separation of geochemical anomalies from background. *J Geochem Explor*. 77: 167-175.

[10]. Panahi, A., Cheng, Q. and Bonham-Carter, G.F. (2004). Modelling lake sediment geochemical distribution using principal component, indicator kriging and multifractal power-spectrum analysis: a case study from Gowganda, Ontario. *Geochem. Explor. Environ. Anal*. 4: 59-70.

[11]. Wang, W., Zhao, J., Cheng, Q. and Liu, J. (2012). Tectonic-geochemical exploration modeling for characterizing geo-anomalies in southeastern Yunnan district, China. *J Geochem Explor*. 122: 71-80.

[12]. Wang, G., Zhang, S., Yan, C., Xu, G., Ma, M. and Li, K. (2012). Application of the multifractal singular value decomposition for delineating geophysical anomalies associated with molybdenum occurrences in the Luanchuan ore field (China). *J. Appl. Geophys*. 86: 109-119.

[13]. Alt-Epping, P. and Zhao, C. (2010). Reactive mass transport modelling of a three-dimensional vertical fault zone with a finger-like convective flow regime. *J Geochem Explor*. 106: 8-23.

[14]. Zhao, C., Hobbs, B., Ord, A. and Peng, S. (2010). Effects of mineral dissolution ratios on chemical-dissolution front instability in fluid-saturated porous media. *Transp. Porous Media*. 82: 317-335.

[15]. Zhao, C., Hobbs, B.E. and Ord, A. (2010). Theoretical and numerical investigation into roles of geofluid flow in ore forming systems: integrated mass conservation and generic model approach. *J Geochem Explor*. 106: 251-260.

- [16]. Liu, L., Wan, C., Zhao, C. and Zhao, Y. (2011). Geodynamic constraints on orebody localization in the Anqing orefield, China: computational modeling and facilitating predictive exploration of deep deposits. *Ore Geol. Rev.* 43: 249-263.
- [17]. He, J.Z., Yao, S.Z., Zhang, Z.P. and You, G.J. (2013). Complexity and productivity differentiation models of metallogenic indicator elements in rocks and supergene media around Daijiazhuang Pb–Zn deposit in Dangchang County, Gansu Province. *Nat. Resour. Res.* 22: 19-36.
- [18]. Gonçalves, M.A. (2001). Characterization of geochemical distributions using multifractal models. *Math. Geol.* 33: 41-61.
- [19]. Reimann, C., Filzmoser, P. and Garrett, R.G. (2005). Background and threshold: critical comparison of methods of determination. *Sci. Total Environ.* 346: 1-16.
- [20]. Gałuszka, A. (2007). A review of geochemical background concepts and an example using data from Poland. *Environ. Geol.* 52: 861-870.
- [21]. Shuguang, Z., Kefa, Z., Yao, C., Jinlin, W. and Jianli, D. (2015). Exploratory data analysis and singularity mapping in geochemical anomaly identification in Karamay, Xinjiang, China. *J Geochem Explor.* 154: 171-179.
- [22]. Geranian, H., Mokhtari, A.R. and Cohen, D.R. (2013). A comparison of fractal methods and probability plots in identifying and mapping soil metal contamination near an active mining area, Iran. *Sci. Total Environ.* 463: 845-854.
- [23]. Zuo, R., Xia, Q. and Wang, H. (2013). Compositional data analysis in the study of integrated geochemical anomalies associated with mineralization. *Appl. Geochem.* 28: 202-211.
- [24]. Zuo, R., Xia, Q. and Zhang, D. (2013). A comparison study of the C–A and S–A models with singularity analysis to identify geochemical anomalies in covered areas. *Appl. Geochem.* 33: 165-172.
- [25]. Zuo, R. (2014). Identification of weak geochemical anomalies using robust neighborhood statistics coupled with GIS in covered areas. *J Geochem Explor.* 136: 93-101.
- [26]. Kafadar, K. and Spiegelman, C.H. (1986). An alternative to ordinary qq plots: Conditional qq plots. *Computational Statistics & Data Analysis.* 4: 167-184.
- [27]. Papastergios, G., Fernandez-Turiel, J.L., Filippidis, A. and Gimeno, D. (2011). Determination of geochemical background for environmental studies of soils via the use of HNO₃ extraction and Q–Q plots. *Env Earth Sci.* 64: 743-751.
- [28]. Boylan, G.L. and Cho, B.R. (2012). The normal probability plot as a tool for understanding data: a shape analysis from the perspective of skewness, kurtosis, and variability. *Quality and Reliability Engineering International.* 28: 249-264.
- [29]. Chiprés, J., Castro-Larragoitia, J. and Monroy, M. (2009). Exploratory and spatial data analysis (EDA–SDA) for determining regional background levels and anomalies of potentially toxic elements in soils from Catorce–Matehuala, Mexico. *Appl. Geochem.* 24: 1579-1589.
- [30]. Carranza, E.J.M. (2010). Mapping of anomalies in continuous and discrete fields of stream sediment geochemical landscapes. *Geochem. Explor. Environ. Anal.* 10: 171-187.
- [31]. Schwertman, N.C., Owens, M.A. and Adnan, R. (2004). A simple more general boxplot method for identifying outliers. *Comput. Stat. Data Anal.* 47: 165-174.
- [32]. Nazarpour, A., Omran, N.R., Paydar, G.R., Sadeghi, B., Matroud, F. and Nejad, A.M. (2015). Application of classical statistics, logratio transformation and multifractal approaches to delineate geochemical anomalies in the Zarshuran gold district, NW Iran. *Chem. Erde.* 75: 117-132.
- [33]. Schwertman, N.C. and De Silva, R. (2007). Identifying outliers with sequential fences. *Comput. Stat. Data Anal.* 51: 3800-3810.
- [34]. Sun, X., Deng, J., Gong, Q., Wang, Q., Yang, L. and Zhao, Z. (2009). Kohonen neural network and factor analysis based approach to geochemical data pattern recognition. *J Geochem Explor.* 103: 6-16.
- [35]. Wang, C., Carranza, E.J.M., Zhang, S., Zhang, J., Liu, X. and Zhang, D. (2013). Characterization of primary geochemical haloes for gold exploration at the Huanxiangwa gold deposit, China. *J Geochem Explor.* 124: 40-58.
- [36]. Meigoony, M.S., Afzal, P., Gholinejad, M., Yasrebi, A.B. and Sadeghi, B. (2014). Delineation of geochemical anomalies using factor analysis and multifractal modeling based on stream sediments data in Sarajeh 1: 100,000 sheet, Central Iran. *Arabian J. Geosci.* 7: 5333-5343.
- [37]. Mohammadi, N.M., Hezarkhani, A. and Saljoughi, B.S. (2016). Separation of a geochemical anomaly from background by fractal and U-statistic methods, a case study: Khooni district, Central Iran. *Chem. Erde.* 76: 491-499.
- [38]. Zhao, J., Chen, S. and Zuo, R. (2016). Identifying geochemical anomalies associated with Au–Cu mineralization using multifractal and artificial neural network models in the Ningqiang district, Shaanxi, China. *J Geochem Explor.* 164: 54-64.
- [39]. Bao, Z., Li, F. and Jia, X. (1999). Methodology of temporal-spatial structure of geochemical fields. *Earth Sci J.* 24: 282-286.

- [40]. Chen, G. and Cheng, Q. (2016). Singularity analysis based on wavelet transform of fractal measures for identifying geochemical anomaly in mineral exploration. *Comput Geosci.* 87: 56-66.
- [41]. Bakaç, M., Kumru, M. and Başsarı, A. (1999). R-mode factor analysis applied to the exploration of radioactivity in the Gediz River. *J. Radioanal. Nucl. Chem.* 242: 457-465.
- [42]. Zuo, R. and Cheng, Q. (2008). Mapping singularities—a technique to identify potential Cu mineral deposits using sediment geochemical data, an example for Tibet, west China. *Mineral. Mag.* 72: 531-534.
- [43]. Mandelbrot, B.B. and Pignoni, R. (1983). *The fractal geometry of nature*: WH freeman New York.
- [44]. Deng, J., Wang, Q., Huang, D., Wan, L., Yang, L. and Gao, B. (2006). Transport network and flow mechanism of shallow ore-bearing magma in Tongling ore cluster area. *Science in China Series D: Earth Sci.* 49: 397-407.
- [45]. Asadi, H.H., Kianpouryan, S., L.u., Y.J. and McCuaig, T.C. (2014). Exploratory data analysis and C–A fractal model applied in mapping multi-element soil anomalies for drilling: A case study from the Sari Gunay epithermal gold deposit, NW Iran. *J Geochem Explor.* 145: 233-241.
- [46]. Ali, K., Cheng, Q. and Chen, Z. (2007). Multifractal power spectrum and singularity analysis for modelling stream sediment geochemical distribution patterns to identify anomalies related to gold mineralization in Yunnan Province, South China. *Geochemistry: Explor. Env. Anal.* 7: 293-301.
- [47]. Afzal, P., Harati, H., Alghalandis, Y.F. and Yasrebi, A.B. (2013). Application of spectrum–area fractal model to identify of geochemical anomalies based on soil data in Kahang porphyry-type Cu deposit, Iran. *Chemie der Erde.* 73: 533-543.
- [48]. Zhao, B. and Chen, Y. (2011). Singular value decomposition (SVD) for extraction of gravity anomaly associated with gold mineralization in Tongshi gold field, Western Shandong Uplifted Block, Eastern China. *Nonlinear Processes Geophys.* 18: 103-109.
- [49]. Mohammadi, A., Khakzad, A., Omran, N.R., Mahvi, M.R., Moarefvand, P. and Afzal, P. (2013). Application of number–size (NS) fractal model for separation of mineralized zones in Dareh-Ashki gold deposit, Muteh Complex, Central Iran. *Arabian J. Geosci.* 6: 4387-4398.
- [50]. Cheng, Q. and Zhao, P. (2011). Singularity theories and methods for characterizing mineralization processes and mapping geo-anomalies for mineral deposit prediction. *Geosci. Front.* 2: 67-79.
- [51]. Shuyun, X., Qiuming, C., Xianzhong, K., Zhengyu, B., Changming, W. and Haoli, Q. (2008). Identification of geochemical anomaly by multifractal analysis. *J China Uni Geosci.* 19: 334-342.
- [52]. Arias, M., Gumiel, P., Sanderson, D.J. and Martin-Izard, A. (2011). A multifractal simulation model for the distribution of VMS deposits in the Spanish segment of the Iberian Pyrite Belt. *Comput Geosci.* 37: 1917-1927.
- [53]. Sun, X., Gong, Q., Wang, Q., Yang, L., Wang, C. and Wang, Z. (2010). Application of local singularity model to delineate geochemical anomalies in Xiong'ershan gold and molybdenum ore district, Western Henan province, China. *J Geochem Explor.* 107: 21-29.
- [54]. Ziaii, M., Ardejani, F.D., Ziaei, M. and Soleymani, A.A. (2012). Neuro-fuzzy modeling based genetic algorithms for identification of geochemical anomalies in mining geochemistry. *Appl. Geochem.* 27: 663-676.
- [55]. Xiong, Y. and Zuo, R. (2016). Recognition of geochemical anomalies using a deep autoencoder network. *Comput Geosci.* 86: 75-82.
- [56]. Geological Survey of Iran. (1973). Exploration for ore deposits in Kerman region, Report no. Yu/53.
- [57]. Dimitrijevic, M.D. (1973). Geology of the Kerman region, Report no. Yu/52. Geological Survey of Iran, Iran.
- [58]. Xiao, F., Chen, J., Zhang, Z., Wang, C., Wu, G. and Agterberg, F.P. (2012). Singularity mapping and spatially weighted principal component analysis to identify geochemical anomalies associated with Ag and Pb-Zn polymetallic mineralization in Northwest Zhejiang, China. *J Geochem Explor.* 122: 90-100.
- [59]. Liu, Y., Cheng, Q., Xia, Q. and Wang, X. (2013). Application of singularity analysis for mineral potential identification using geochemical data—A case study: Nanling W–Sn–Mo polymetallic metallogenic belt, South China. *J Geochem Explor.* 134: 61-72.
- [60]. Lou, D., Zhang, C. and Liu, H. (2015). The multifractal nature of the Ni geochemical field and implications for potential Ni mineral resources in the Huangshan–Jing'erquan area, Xinjiang, China. *J Geochem Explor.* 157: 169-177.
- [61]. Muller, J., Kylander, M., Martinez-Cortizas, A., Wüst, R.A., Weiss, D. and Blake, K. (2008). The use of principle component analyses in characterising trace and major elemental distribution in a 55kyr peat deposit in tropical Australia: implications to paleoclimate. *Geochim. Cosmochim. Acta.* 72: 449-463.
- [62]. Johnson, R.A. and Wichern, D.W. (2014). *Applied multivariate statistical analysis*: Prentice-Hall New Jersey.
- [63]. Um, M.J., Yun, H., Jeong, C.S. and Heo, J.H. (2011). Factor analysis and multiple regression

between topography and precipitation on Jeju Island, Korea. *J. Hydrol.* 410: 189-203.

[64]. Filzmoser, P. and Todorov, V. (2011). Review of robust multivariate statistical methods in high dimension. *Anal. Chim. Acta.* 705: 2-14.

[65]. Rousseeuw, P.J. and Driessen, K.V. (1999). A fast algorithm for the minimum covariance determinant estimator. *Technometrics.* 41: 212-223.

[66]. Yang, X. and Han, H. (2017). Factors analysis of protein O-glycosylation site prediction. *Comput. Biol. Chem.*

[67]. Chayes, F. (1960). On correlation between variables of constant sum. *J. Geophys. Res.* 65: 4185-4193.

[68]. Egozcue, J.J., Pawlowsky-Glahn, V., Mateu-Figueras, G. and Barcelo-Vidal, C. (2003). Isometric logratio transformations for compositional data analysis. *Math. Geol.* 35: 279-300.

[69]. Xu, Y. and Cheng, Q. (2001). A fractal filtering technique for processing regional geochemical maps for mineral exploration. *Geochem. Explor. Environ. Anal.* 1: 147-156.

[70]. Cheng, Q., Xu, Y. and Grunsky, E. (1999). Integrated spatial and spectral analysis for geochemical anomaly separation, August 6-11. 6th Annual Conference of the International Association for Math. Geol, Trondheim, Norway.

[71]. Ge, Y., Cheng, Q. and Zhang, S. (2005). Reduction of edge effects in spatial information extraction from regional geochemical data: a case study based on multifractal filtering technique. *Comput Geosci.* 31: 545-554.

[72]. Afzal, P., Alghalandis, Y.F., Moarefvand, P., Omran, N.R. and Haroni, H.A. (2012). Application of power-spectrum-volume fractal method for detecting hypogene, supergene enrichment, leached and barren zones in Kahang Cu porphyry deposit, Central Iran. *J Geochem Explor.* 112: 131-138.

[73]. Afzal, P., Ahmadi, K. and Rahbar, K. (2017). Application of fractal-wavelet analysis for separation of geochemical anomalies. *J Afr Earth Sci.* 128: 27-36.

[74]. Daugman, J.G. (1988). Complete discrete 2-D Gabor transforms by neural networks for image analysis and compression. *IEEE Transactions on Acoustics, Speech, and Signal Processing.* 36: 1169-1179.

[75]. Zhang, Z. (2009). Iterative algorithm of wavelet network learning from nonuniform data. *Neurocomputing.* 72: 2979-2999.

[76]. Thuillard, M. (2002). A review of wavelet networks, wavenets, fuzzy wavenets and their applications. *Advances in computational intelligence and learning.* pp. 43-60.

[77]. Zhang, Q. and Benveniste, A. (1992). Wavelet networks. *IEEE transactions on Neural Networks.* 3: 889-898.

[78]. Polycarpou, M.M., Mears, M.J. and Weaver, S.E. (1997). Adaptive wavelet control of nonlinear systems. *Decision and Control, 1997, Proceedings of the 36th IEEE Conference on: IEEE.* pp. 3890-3895.

[79]. Peng, Z., Chu, F. and He, Y. (2002). Vibration signal analysis and feature extraction based on reassigned wavelet scalogram. *J. Sound Vib.* 253: 1087-1100.

[80]. Oussar, Y., Rivals, I., Personnaz, L. and Dreyfus, G. (1998). Training wavelet networks for nonlinear dynamic input-output modeling. *Neurocomputing.* 20: 173-188.

[81]. Oussar, Y. and Dreyfus, G. (2000). Initialization by selection for wavelet network training. *Neurocomputing.* 34: 131-143.

[82]. Alexandridis, A.K. and Zaprani, A.D. (2013). Wavelet neural networks: A practical guide. *Neural Net.* 42: 1-27.

[83]. Hezarkhani, A. (2008). Hydrothermal evolution of the Miduk porphyry copper system, Kerman, Iran: a fluid inclusion investigation. *Int. Geol. Rev.* 50: 665-684.

[84]. Mahmoudabadi, H., Izadi, M. and Menhaj, M.B. (2009). A hybrid method for grade estimation using genetic algorithm and neural networks. *Comput. Geosci.* 13: 91-101.

[85]. Li, X.L., Li, L.H., Zhang, B.L. and Guo, Q.J. (2013). Hybrid self-adaptive learning based particle swarm optimization and support vector regression model for grade estimation. *Neurocomputing.* 118: 179-190.

[86]. Sola, J. and Sevilla, J. (1997). Importance of input data normalization for the application of neural networks to complex industrial problems. *IEEE Transactions on Nuclear Science.* 44: 1464-1468.

[87]. Kasiviswanathan, K., He, J., Sudheer, K. and Tay, J.H. (2016). Potential application of wavelet neural network ensemble to forecast streamflow for flood management. *J. Hydrol.* 536: 161-173.

[88]. Crochemore, L., Perrin, C., Andréassian, V., Ehret, U., Seibert, S.P. and Grimaldi, S. (2015). Comparing expert judgement and numerical criteria for hydrograph evaluation. *Hydrol. Sci. J.* 60: 402-423.

[89]. Sreekanth, P., Geethanjali, N., Sreedevi, P., Ahmed, S., Kumar, N.R. and Jayanthi, P.K. (2009). Forecasting groundwater level using artificial neural networks. *Current sci.* pp. 933-939.

[90]. Pourtaghi, A. and Lotfollahi-Yaghin, M. (2012). Wavenet ability assessment in comparison to ANN for predicting the maximum surface settlement caused by

tunneling. *Tunnelling Underground Space Technol.* 28: 257-271.

[91]. Tangestani, M.H., Mazhari, N., Agar, B. and Moore, F. (2008). Evaluating Advanced Spaceborne Thermal Emission and Reflection Radiometer (ASTER) data for alteration zone enhancement in a

semi-arid area, northern Shahr-e-Babak, SE Iran. *Int. J. Remote Sens.* 29: 2833-2850.

[92]. Tangestani, M.H. and Moore, F. (2002). The use of Dempster-Shafer model and GIS in integration of geoscientific data for porphyry copper potential mapping, north of Shahr-e-Babak, Iran. *Int. J. Appl. Earth Obs. Geoinf.* 4: 65-74.

شناسایی آنومالی‌های ژئوشیمیایی مرتبط با کانی‌زایی مس توسط روش‌های چند فرکتال طیف توان- مساحت و شبکه عصبی موجک در ناحیه معدنی شهر بابک، کرمان، ایران

بشیر شکوه سلجوقی و اردشیر هزارخانی*

دانشکده مهندسی معدن و متالورژی، دانشگاه صنعتی امیرکبیر، ایران

ارسال ۲۰۱۸/۴/۷، پذیرش ۲۰۱۸/۷/۲۱

* نویسنده مسئول مکاتبات: ardehez@aut.ac.ir

چکیده:

ناحیه شهر بابک به عنوان ناحیه مطالعاتی به خاطر منابع عظیم مس خود شناخته شده است. این ناحیه در بخش جنوبی کمپلکس آتشفشانی- رسوبی ایران مرکزی در جنوب شرق ایران واقع شده است. ناحیه شهر بابک در حال حاضر مواجه با کمبود منابع است، بنابراین اکتشاف مواد معدنی در فضاهای عمیق تر و پیرامونی اولویت اصلی در این ناحیه است. این پژوهش قصد در شناسایی آنومالی‌های ژئوشیمیایی مرتبط با کانی‌سازی مس با استفاده از روش‌های چند فرکتال طیف توان- مساحت و شبکه عصبی موجک دارد. در ابتدا، تجزیه و تحلیل عاملی برای تلفیق متغیرهای ژئوشیمیایی چندگانه با دسته داده رسوبات آبراهه‌ای مرتبط با عناصر اصلی کانی‌زایی در ناحیه مطالعاتی به کار برده شد. سپس روش طیف توان- مساحت برای تجزیه الگوهای ژئوشیمیایی مختلط به دست آمده از تجزیه و تحلیل عاملی و مقایسه با نتایج به دست آمده از روش شبکه عصبی موجک استفاده شد. مدل طیف توان- مساحت مبتنی بر خواص مقیاس‌بندی ناهمسانگردی مجزا، آنومالی‌های محلی را با توجه به مشخصات فضایی متغیرهای ژئوشیمیایی آشکار کرد. اغلب محققان نشان دادند که قابلیت‌های شبکه عصبی مصنوعی (یعنی طبقه‌بندی، تطابق الگو، بهینه‌سازی و پیش‌بینی) با توجه به کاربرد موفقیت‌آمیزش، برای عدم قطعیت‌های ذاتی و کاستی‌ها موجود در مسائل مهندسی معدن مناسب است. در این پژوهش، یک روش جایگزین شبکه عصبی مصنوعی به نام شبکه عصبی موجک برای پی‌جویی معدنی مبتنی بر ترکیب تئوری موجک و شبکه عصبی مصنوعی ارائه شده است. نتایج به دست آمده از روش شبکه عصبی موجک در تطابق خوب با نهشته‌های شناخته شده، نشان می‌دهد که روش شبکه عصبی موجک با تابع انتقال مورلت توانایی بالایی برای یادگیری و شناخت سامانه‌های پیچیده تعریف نشده و نامعین دارد. روش ترکیبی تجزیه و تحلیل عاملی، طیف توان- مساحت و شبکه عصبی موجک به کار برده شده در این مطالعه برای شناسایی آنومالی‌های مرتبط با کانی‌زایی مس برای اکتشاف آتی منابع معدنی سودمند است.

کلمات کلیدی: آنومالی ژئوشیمیایی، شبکه عصبی موجک، مدل چند فرکتال طیف توان- مساحت، کانی‌زایی مس، شهر بابک.